

Towards a realistic noise modelling of quantum sensors for future satellite gravity missions

João Encarnação^{a,*}, Christian Siemes^a, Ilias Daras^b, Olivier Carraz^b, Aaron Strangfeld^b, Philipp Zingerle^c, Roland Pail^c

^a Delft University of Technology, Kluyverweg 1, 2629 HS, Delft, the Netherlands

^b European Space Research and Technology Centre, Keplerlaan 1, 2200 AG Noordwijk, the Netherlands

^c Technical University of Munich, Arcisstraße 21, D-80333 Munich, Germany

Abstract

Cold Atom Interferometry (CAI) accelerometers and gradiometers have emerged as promising candidates for future gravimetric satellite missions due to their potential for detecting gravitational forces and gradients with high precision and accuracy. Space-based quantum technology has the potential to revolutionise Earth observation and monitoring. Mapping the Earth's gravity field from space offers valuable insights into climate change, hydro- and biosphere evolution, and seismic activity prediction. Current satellite gravimetry missions have demonstrated the utility of gravity data in understanding global mass transport phenomena, climate dynamics, and geological processes. However, state-of-the-art measurement techniques face noise and long-term drift limitations, which might propagate on the recovery of Earth's time-varying gravity field. Quantum sensors, particularly atom interferometry-based devices, offer promise for improving the accuracy and stability of space-based gravity measurements. This study explores the sensitivity of CAI accelerometers and gradiometers, considering parameters such as interferometry contrast, degree of entanglement, number of atoms, momentum space separation, and interrogation period. We explore the low-low satellite-to-satellite and gravity gradiometry measurements to build analytical models of measurements and associated errors. We selected an ambitious scenario for CAI parameters that illustrates a potential path for increasing instrument accuracies and capabilities for space gravimetry. Two operational modes, concurrent and sequential, are compared to mitigate the effects of inaccurately known attitude rates on Coriolis accelerations. The sequential mode shows the potential to reduce these effects, enabling accurate measurements for low-low Satellite-to-Satellite Tracking (ll-SST) missions in the near future. Attitude determination is discussed, highlighting the importance of accurate measurements to reconstruct Coriolis accelerations and related to errors in the reference frame rotation from body or local frames to the Earth co-rotating frame. We find it essential to understand and navigate the inherent technical challenges associated with quantum sensors to secure a realistic path towards exploiting this technology to understand the gravity field.

* Corresponding author.

Email address: J.G.deTeixeiradaEncarnacao@tudelft.nl

1 Introduction

Recent advancements in quantum technology have spurred interest in developing highly sensitive instruments for gravitational measurements from space. Among these instruments, Cold Atom Interferometry (CAI) accelerometers and gradiometers are promising due to their potential for observing gravitational forces and gradients with high precision and accuracy. The microgravity environment in space allows for substantially longer interrogation time than on the ground, which is currently a limitation in developing these instruments.

The European Commission, backed by several European countries, has recently announced substantial investments in quantum technology (QT) to tackle contemporary digital challenges, including secure communication and computing power. Europe has been at the forefront of spaceborne quantum sensor development since the early 2000s, with initiatives such as the *Interférométrie atomique à sources Cohérentes pour l'Espace* (ICE) and *Matter-Wave Interferometry in Weightlessness* (MAIUS) advancing the field. The development of quantum sensors requires close collaboration between academia, industry, and space agencies to overcome technological challenges and prepare for future space missions (Kaltenbaek et al. 2021). Furthermore, integrating quantum sensors in space missions might enhance Earth observation and facilitate the exploration of celestial bodies like the Moon and Mars, ushering in a new era of space science and technology (Abend et al. 2023).

Mapping the Earth's gravity field from space offers unique insights into climate change, hydro and cryosphere evolution (Groh et al. 2019; Jiang et al. 2014), and seismic activity monitoring and modelling (Han 2006), amongst others. Past satellite gravimetry missions, such as NASA's GRACE and ESA's GOCE, have demonstrated the utility of gravity data in understanding global mass transport phenomena, climate dynamics, and geological processes. However, classical measurement techniques face limitations regarding noise and drifts, which might propagate on the recovery of Earth's time-varying gravity field. ESA's *Next Generation Gravity Mission* (NGGM) and NASA's Mass Change mission are poised to leverage classic sensors to enhance Earth observation capabilities (Massotti et al. 2021; Cesare et al. 2022; Heller-Kaikov, Pail, and Daras 2023). The advent of quantum sensors, particularly atom interferometry-based devices, holds promise for improving the accuracy and stability of space-based gravity measurements.

This study intends to describe and motivate the most relevant error specifications for Quantum Space Gravimetry (QSG), including interferometry contrast, degree of entanglement, number of atoms, momentum space separation, and interrogation period. Our analyses include the relevant gravimetric instruments related to attitude, Inter-satellite Ranging (ISR), and acceleration sensors. We also investigate the effect of inaccurately known attitude to the Coriolis accelerations and propose mitigation strategies. We also quantify the impact of reference frame transformations of the measurements in the presence of inaccurate attitude information. While we are not proposing any specific mission configuration, we investigate several measurement concepts that could be realised within the next two decades and quantify the relevant error components.

To retain a clear focus on the instrument design and to limit the extent, we perform no further analyses of the impact of the developed instrument noise models on concrete satellite gravity missions. For that, we refer to Zingerle et al. (2014), who present the propagation of the predicted noise spectra to the gravity field coefficients. That study puts the sensor errors in context with other sources of errors that we are unable to consider, notably temporal aliasing

and presents a broad collection of possible future satellite gravity constellation scenarios. Both studies are part of the same ESA QSG4EMT project; see acknowledgements. The results presented in this study are part of the sensitivity analysis of quantum instrument performances, which was fed into the trade space analysis of QSG mission architectures in conjunction with a consolidated user requirements database for future QSG missions.

We consider two measurement concepts: changes in the range between two satellites orbiting in formation, a technique called low-low Satellite-to-Satellite (ll-SST), and in situ gravity gradients collected by a gradiometer onboard a single satellite, called Gravity Gradiometry (GG). In the case of ll-SST, the changes in the inter-satellite range are caused by gravity and non-gravitational accelerations affecting the motion of the satellites. This measurement concept requires accelerometers that are by design sensitive to non-gravitational accelerations, allowing the gravitational accelerations to be isolated. In the case of GG, the gradiometer comprises one or more pairs of accelerometers, and their differential acceleration measurements are related to the gravity gradient at that location. We designate the accelerometers onboard current and past gravimetric missions by electrostatic instruments, cf. Section 2.3.1 and *quantum* instruments are those that have been proposed to succeed the former, further discussed in Section 2.3.2. Associated with the measured inter-satellite ranges and gravity gradients of these measurement concepts are their respective *product noise*, which is a function of the sensitivity of the relevant sensors and auxiliary instruments, such as those that collected information related to the attitude and position relative to Earth.

We describe the errors with Amplitude Spectral Densities (ASD) to which we associate the symbol σ in the relevant equations. Based on the instrument noise described in Section 2, we assess the product noise in Section 3, which results from error propagation through the observation equations of electrostatic and quantum instruments applied to ll-SST and GG measurement concepts. We also describe the effect of imperfect attitude reconstruction in the product noise in Section 4. Section 5 presents the results and numerical quantification of our assumptions and models.

Overall, this study shall lay the groundwork for future developments in quantum gravimetry and, consequently, future satellite missions, highlighting the importance of accurately measuring the satellite's angular velocity and leveraging advancements in laser metrology to achieve unprecedented levels of precision in gravitational measurements.

2 Instrument specifications

We present in this section the noise ASD of all sensors we consider in this study, including the star sensors, differential wavefront sensors (DWS), K-band ranging instrument (KBR), laser ranging interferometer (LRI), electrostatic accelerometers, laser gyroscopes, and predicted CAI instruments. We subdivide into attitude sensors, ranging instruments, electrostatic and quantum accelerometers.

We provide a non-exhaustive list of sensors that are representative of state-of-the-art technology. In the case of the ll-SST, we also provide the expected performance of the laser ranging instrument in the foreseeable future.

Multiple sensors that measure the same quantity may be installed in future gravimetric missions. In that case, we assume that m different instruments with error spectra are combined optimally, similar to the combination of attitude sensors by Stummer, Fecher, and Pail (2011):

$$\sigma^2(f) = \left(\sum_{m=1}^M \sigma_m^{-2}(f) \right)^{-1}. \quad (1)$$

Here, $\sigma_m(f)$ is the noise ASD of sensor m , and $\sigma(f)$ is the noise ASD when all sensors are combined optimally. We use the symbol σ to identify the frequency-dependent errors, even if omitting the dependency of frequency, e.g., σ .

Integration or differentiation of the noise ASD of a quantity requires the factor $2\pi f$ or its inverse, respectively. In the general case of the n -th derivative ($n > 0$) or n -th integral ($n < 0$), using Lagrange's notation for differentiation and antidifferentiation:

$$\sigma(f^{(n)}) = (2\pi f)^n \sigma(f). \quad (2)$$

2.1 Attitude Sensors

This section presents the noise ASD of the attitude instruments considered in the study. We present a wide selection of attitude instruments to assess what is technically feasible in the foreseeable future. Figure 1 shows an overview of the attitude noise ASDs, where all quantities have been converted to attitude (left) and angular rates (right) for convenience.

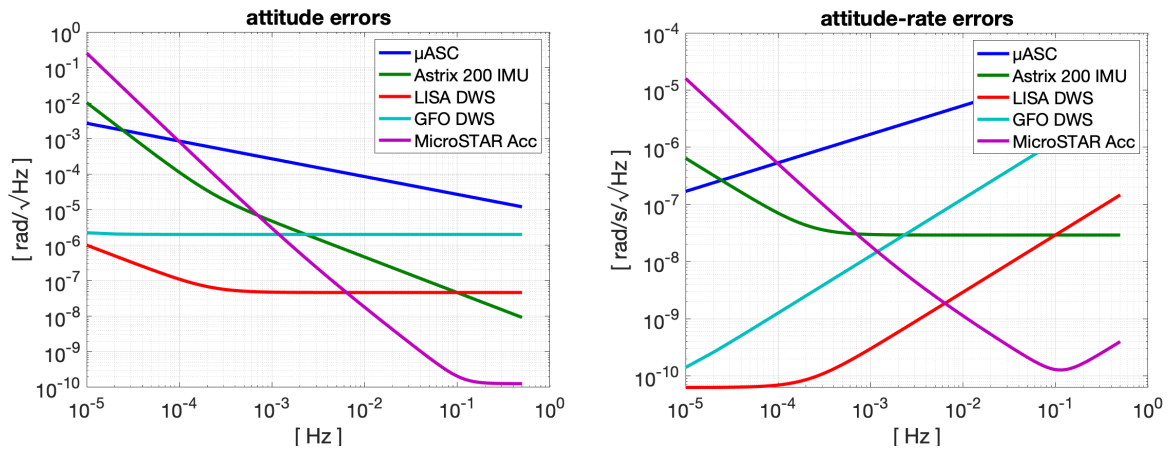


Figure 1: Overview of attitude errors in terms of attitude (left) and angular rates (right).

To clarify our notation, the symbols σ_θ , σ_ω and $\sigma_{\dot{\omega}}$ relate to angular, angular rate and angular acceleration errors, respectively.

2.1.1 Star tracker

The star sensor of the Swarm satellites is the Micro Advanced Stellar Compass (μ ASC) (Herceg, Jørgensen, and Jørgensen 2017). We believe that this instrument is a representative state-of-the-art star sensor. Goswami et al. (2021) analysed its in-flight accuracy and specified that noise ASD as

$$\sigma_{\mu\text{ASC},\theta}(f) = 8.5 \times 10^{-6} \sqrt{f^{-1}} \left[\frac{\text{rad}}{\sqrt{\text{Hz}}} \right]. \quad (3)$$

2.1.2 Inertial Measurement Unit

One of the most accurate inertial measurement units (IMU) is the Astrix 200 laser gyroscope, the accuracy of which is specified by Airbus (2022). It has a white noise component of 3×10^{-8} rad/s and a f^{-1} component associated with a bias drift, as shown in Figure 2. The combined analytical expression is

$$\sigma_{\text{IMU},\omega}(f) = 3 \times 10^{-8} \sqrt{1 + 4.6 \times 10^{-8} f^{-2}} \left[\frac{\text{rad/s}}{\sqrt{\text{Hz}}} \right]. \quad (4)$$

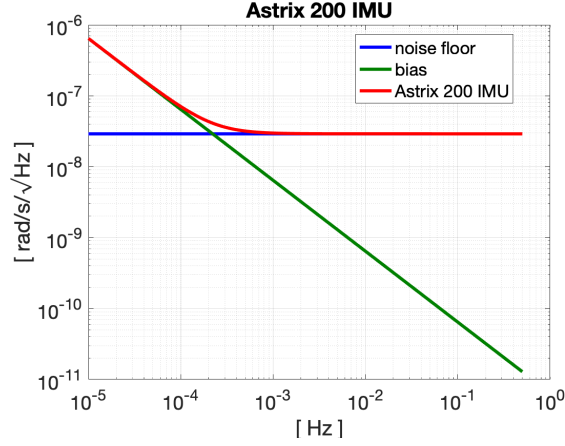


Figure 2: ASD of the angular velocity noise of the Astrix 200 IMU as inferred from Airbus (2022).

2.1.3 Differential Wave Sensor

The DWS measures pitch and yaw relative to the inter-satellite laser. In combination with the GNSS-derived positions, it is possible to derive the absolute pitch and yaw attitude of the satellite because the GNSS positions provide the absolute attitude of the vector connecting the two satellites. The DWS noise spectra are provided for two cases in the following sections. As for the errors in GNSS σ_{GNSS} (supposing white noise with an amplitude of 1 cm), they proportionally affect the attitude error in the Line-Of-Sight (LOS) unit vector $\sigma_{\text{LOS},\theta}$. Finally, this effect is dampened proportionally to the inter-satellite distance L_{ISR} , assumed to be 200km:

$$\sigma_{\text{LOS},\theta} = \frac{\sigma_{\text{GNSS}}}{L_{\text{ISR}}} \cong 5 \times 10^{-8} \left[\frac{\text{rad}}{\sqrt{\text{Hz}}} \right]. \quad (5)$$

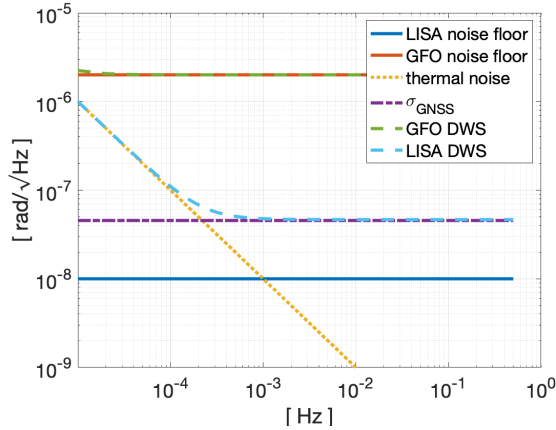


Figure 3: ASD of the attitude errors for the DWS of LISA (dashed blue line), based on Schütze et al. (2013) and for the DWS of GRACE-FO (dashed green line), adapted from (Goswami et al. 2021).

2.1.3.1 LISA

For LISA, the noise ASD of the DWS is taken from Schütze et al. (2013). As shown in Figure 3, it is composed of the white noise floor (solid blue line) at the level of $10 \text{ nrad}/\sqrt{\text{Hz}}$ between 1mHz and 1 Hz and the thermal noise (dotted yellow line) with a spectrum of $1/f$ below 1 mHz.

2.1.3.2 GRACE-FO

Referring to Figure 3, for GRACE-FO, it is also possible to derive an estimate for the DWS-derived pitch and yaw attitude errors considering the white noise floor (red line) reported by Goswami et al. (2021), which has an amplitude of $2 \text{ } \mu\text{rad}/\sqrt{\text{Hz}}$. The thermal noise floor (dotted yellow line) and the attitude error of the LOS unit vector (dot-dashed purple line) are

assumed to be equal to the LISA case in Section 2.1.3.1. The noise floor of the DWS sensor is dominant over the GNSS and the thermal components in contrast to the DWS of LISA.

2.1.4 Accelerometer-derived attitude

Since each facet of the proof-mass cavity contains multiple electrodes, the MicroSTAR accelerometer can measure angular accelerations, with error amplitude reported by Christophe et al. (2018). The associated analytical expression for the ASD is:

$$\sigma_{\text{MicroSTAR},\omega}(f) = 1 \times 10^{-10} \sqrt{0.4 + 0.001f^{-1} + 2500f^4} \left[\frac{\text{rad/s}^2}{\sqrt{\text{Hz}}} \right]. \quad (6)$$

We assume this noise ASD is the same for all three axes, considering a cubic proof mass, identical gaps between the proof mass and electrodes on all sides, and neglecting the influence of the gold wire connected to the proof mass needed to neutralise the build-up of static charge.

2.2 Inter-Satellite Ranging

This section presents the noise ASD of the ISR instruments considered in the study. The overview of the noise ASD is shown in Figure 4.

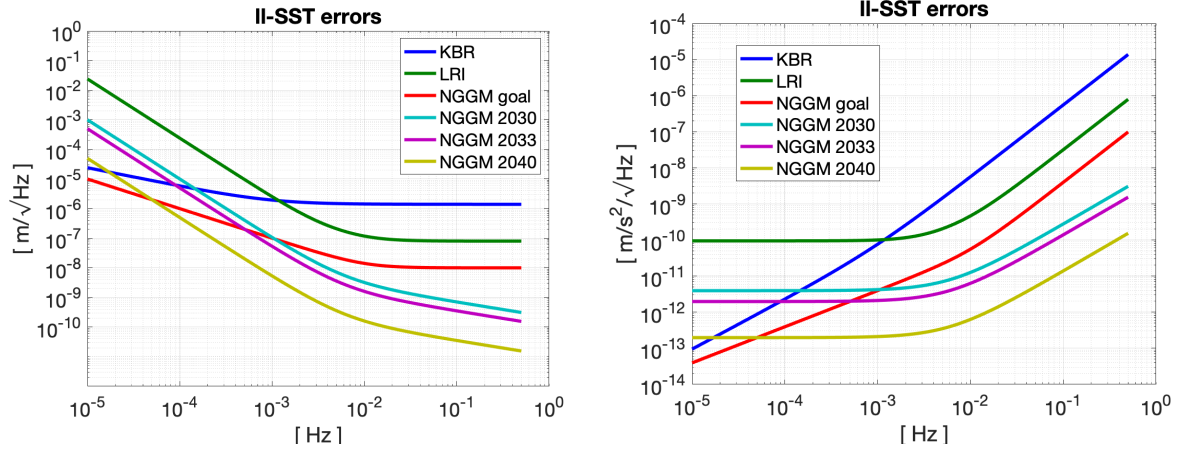


Figure 4: Overview of ISR noise ASD at the level of distance (left) and acceleration (right).

As we intend to quantify the errors for quantum gravimetric missions, which are currently in the early stages of development, we will consider the error spectra associated with the *NGGM 2040* scenario. We report numerous other scenarios for the ranging instrument to contextualise our assumptions with existing instruments and assumptions in the literature.

2.2.1 GRACE-FO KBR

Sheard et al. (2012) provides accuracy of the KBR system. It is composed of thermal and Ultra-Stable Oscillator (USO)-related components described by the analytical expression and illustrated in Figure 5:

$$\begin{aligned} \sigma_{\text{KBR},\rho} &= \sigma_{\text{KBR,thermal}} + \sigma_{\text{KBR,USO}}(f) \\ &= 1.4 \times 10^{-6} \left[\frac{\text{m}}{\sqrt{\text{Hz}}} \right] + 1.8 \times 10^{-8} f^{-1.6} \left[\frac{\text{m}}{\sqrt{\text{Hz}}} \right] \end{aligned} \quad (7)$$

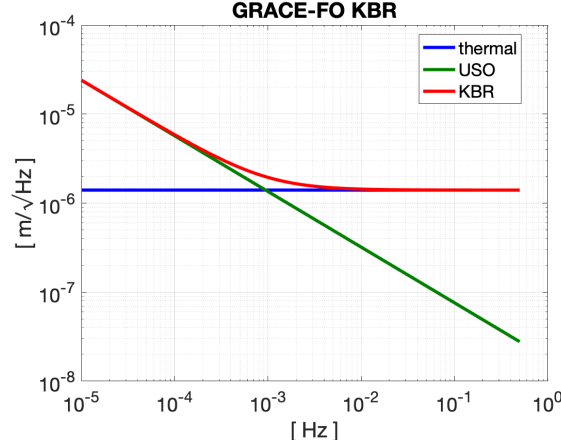


Figure 5: Noise ASD of the GRACE-FO KBR, according to Figure 2 of Sheard et al. (2012).

2.2.2 GRACE-FO LRI

For the noise ASD of the LRI of the GRACE-FO mission, we refer to Kornfeld et al. (2019), which provides the following analytical expression in terms of range noise:

$$\sigma_{\text{LRI},\rho}(f) = 8 \times 10^{-8} \sqrt{1 + (f/0.003)^{-2}} \sqrt{1 + (f/0.01)^{-2}} \left[\frac{m}{\sqrt{\text{Hz}}} \right]. \quad (8)$$

Refer to the green line in Figure 4.

2.2.3 NGGM “goal” LRI

The ISR sensors presented so far are indicative of the existing instruments. A comparison between these and future QSG would not correctly represent the capabilities of the former. For that reason, we include in this study the “goal” performance of the NGGM mission concept proposed by Massotti et al. (2021). The associated analytical expression is a function of the inter-satellite range L_{ISR} :

$$\sigma_{\text{NGGM},\rho}(f) = L_{\text{ISR}} 10^{-13} \sqrt{1 + (0.01/f)^2} \sqrt{1 + (0.001/f)^2} \left[\frac{m}{\sqrt{\text{Hz}}} \right]. \quad (9)$$

Refer to the red line in Figure 4.

2.2.4 NGGM predicted

For the projected accuracy of future ISR laser instruments, we consider the following spectra, which are predicted to be representative of the errors of these instruments at different years (p.c. Vitali Müller, Albert-Einstein-Institut, Hannover, March 2023):

$$\sigma_{\text{NGGM } 2030,\rho}(f) = L_{\text{ISR}} \frac{1 \times 10^{-15}}{f} + \frac{1 \times 10^{-13}}{f^2} \left[\frac{m}{\sqrt{\text{Hz}}} \right], \quad (10)$$

$$\sigma_{\text{NGGM } 2033,\rho}(f) = L_{\text{ISR}} \frac{5 \times 10^{-16}}{f} + \frac{5 \times 10^{-14}}{f^2} \left[\frac{m}{\sqrt{\text{Hz}}} \right], \quad (11)$$

$$\sigma_{\text{NGGM } 2040,\rho}(f) = L_{\text{ISR}} \frac{5 \times 10^{-17}}{f} + \frac{5 \times 10^{-15}}{f^2} \left[\frac{m}{\sqrt{\text{Hz}}} \right]. \quad (12)$$

The subscript indicates the year in which the instrument is predicted to be ready for flight. Refer to the teal, purple and yellow lines, respectively, in Figure 4. We note that Equation (11) is equivalent to Equation (10), considering only thermal noise at low frequency (<1mHz) and, therefore, no dependency on inter-satellite distance at low frequency. Equation (12) is an improvement of factor 2 over Equation (11), as already shown in GRACE-FO

(Abich et al. 2019). Equation (13) is one order of magnitude improvement, as expected by LISA (Dahl et al. 2019).

2.3 Accelerometry

2.3.1 Electrostatic accelerometry

As electrostatic accelerometers, we consider the goal requirements of the NGGM mission concept and the performance of the MicroSTAR accelerometer for the linear acceleration measurements. Figure 6 presents an overview.

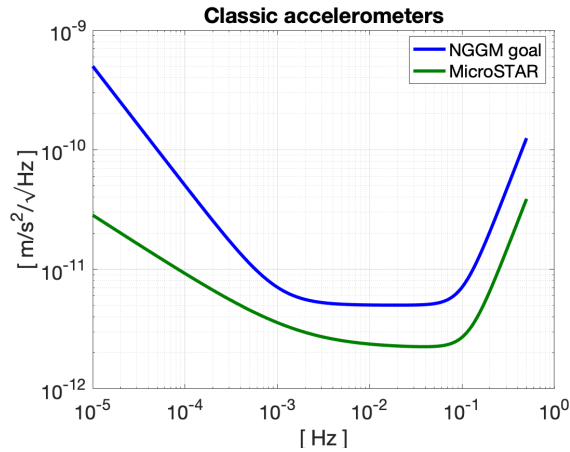


Figure 6: Overview of the noise ASD of electrostatic accelerometers.

2.3.1.1 NGGM “goal” accelerometer

Massotti et al. (2021) reports “goal” and “threshold” requirements for the accelerometer performance of the NGGM mission concept. We selected the “goal” scenario with the associated noise ASD is defined by:

$$\sigma_{\text{NGGM,ng}}(f) = 5 \times 10^{-12} \sqrt{1 + (0.001/f)^2 + (100f^2)^2} \left[\frac{\text{m/s}^2}{\sqrt{\text{Hz}}} \right] \quad (13)$$

2.3.1.2 MicroSTAR

Christophe et al. (2018) provides the MicroSTAR performance, with the noise ASD given by the expression:

$$\sigma_{\text{MicroSTAR,ng}}(f) = 2 \times 10^{-12} \sqrt{1.2 + 0.002f^{-1} + 6000f^4} \left[\frac{\text{m/s}^2}{\sqrt{\text{Hz}}} \right]. \quad (14)$$

2.3.2 Quantum accelerometry

We assume a CAI scheme similar to Malossi et al. (2010):

- i) a Bose-Einstein Condensate (BEC) atomic cloud is produced from a Magneto-Optical Trap (MOT) by laser cooling and magnetic trapping techniques,
- ii) a Raman pulse splits the wave-packet in two, kicking them in opposite directions along the axis of the Raman lasers and over the interrogation period T ,
- iii) a second Raman pulse imparts opposite momentum to the wave-packet, forcing them to converge,
- iv) after the same period of interrogation, a third Raman pulse recombines the wave-packet, and
- v) the interferometric measurement is conducted on the recombined wave-packet.

We use the term *wave-packet* to recognise the wave-particle duality of the BEC because, formally, there is no physical separation of the atomic clouds. Only the wave function is spread in two directions; henceforth, the term (*atom*) *cloud* intends to loosely refer to the physical cloud (in the case of quantum gradiometry in Sections 2.4 and 3.2.2), the BEC and

the wave-packet, except when it is essential to make a distinction. The first and third pulses are also called $\pi/2$ pulses, and the second pulse is called a π pulse. A non-zero acceleration \mathbf{a} along the axis of the Raman laser will induce phase shift ϕ proportional to the acceleration the atom clouds have experienced during $2T$:

$$\phi = \mathbf{k}_{\text{eff}} \cdot \mathbf{a}T^2. \quad (15)$$

The magnitude of effective wavevector k_{eff} is inversely proportional to the wavelength of the Raman laser λ . In the case of the double-diffraction scheme considered in this study, because of the direct and reflected Raman laser:

$$k_{\text{eff}} = \frac{8\pi}{\lambda}. \quad (16)$$

By introducing the degree of entanglement α (e.g. for $\alpha = 0$, there is no entanglement and therefore reaching quantum projection noise; for $\alpha=1$ the Heisenberg limit is attained), with interferometer contrast C and the number of atoms N , the interferometric phase noise is:

$$\sigma_{\phi} = \frac{1}{C} N^{-\frac{1+\alpha}{2}}. \quad (17)$$

The interferometer contrast represents the visibility in which the interferometry fringes appear in the detector. The beam splitting efficiency and any external perturbations influence its value because they lead to a loss of atoms in the phase shift, mainly due to non-inertial effects. Experimental values go from 0.6 (Zhu et al. 2022) or 0.65 (Peters et al. 1999) to $C = 0.8$ (Knabe et al. 2022), while the maximum value is 1 (Douch et al. 2018). The degree of entanglement refers to different quantum enhancement techniques that allow the phase difference after the interrogation time T to be observed more accurately (Szigeti, Hosten, and Haine 2021), with *Spin Squeezing* being the most common (Gross 2012). Parameter α reflects the proportion of atoms in the cloud that are entangled, ranging from 0 to 1, where the value 0 means there is no entanglement.

In the case of concept involving multiple momentum diffraction, the momentum transfer δp is the product of k_{eff} with the Momentum Space Separation β , which has unit value for the baseline double diffraction:

$$\delta p = \hbar\beta k_{\text{eff}} \quad (18)$$

Under these assumptions, with T being the interrogation period, the CAI accelerometer shot-to-shot sensitivity is:

$$\sigma_{\text{CAI,ng}}^{(s2s)} = \frac{\hbar\sigma_{\phi}}{\delta p T^2} = \frac{1}{C\beta k_{\text{eff}} N^{\frac{1+\alpha}{2}} T^2} \quad (19)$$

We assume that the noise spectra of the CAI accelerometers are flat, corresponding to white noise; for this reason, the standard deviation is sufficient to describe these errors entirely.

2.3.2.1 Mode of operation

So far, we have restricted our analysis to the shot-to-shot sensitivity CAI sensitivity, which represents the best-case scenario where the measurements are made continuously without any interruptions. In reality, this is impossible because the atom cloud needs time to be prepared, which we assume to be $T_{\text{prep}} = 1\text{s}$ (Müntinga et al. 2013). Additionally, we define T_{cycle} as the complete measurement cycle period.

We identify two distinct modes for the design and operation of the CAI:

- *Concurrent* atom cloud preparation and interrogation, where the interferometry takes place at the same time as the BEC is being prepared: $T_{\text{cycle}} = T_{\text{prep}}$

- *Sequential* atom cloud preparation and interrogation, the process for cloud preparation and interrogation do not overlap, leading to a more extended measurement cycle period: $T_{\text{cycle}} = 2T + T_{\text{prep}}$.

In the concurrent case, the next atom cloud can be launched before the cold atom interferometer sequence of the current atom cloud is finished, i.e., the measurement cycle T_{cycle} is only limited by the atom cloud preparation time T_{prep} , and we avoid any dead time between measurement cycles.

For both cases, the standard deviation of the CAI acceleration is:

$$\sigma_{\text{CAI,ng}} = \sqrt{T_{\text{cycle}} \sigma_{\text{CAI,ng}}^{(s^2s)}} \quad (20)$$

Additional considerations regarding how the Coriolis accelerations influence both operation modes are discussed in Section 5.1.

One consequence of the two operational modes is the cloud velocity, which will be analysed in Section 5.1. The sequential mode of operation allows for initial zero-atom cloud velocity since the preparation of the BEC and interferometric chambers are placed at the same location. The BEC is directly prepared at the CoM and the wave packet propagates exclusively along the axis of the Raman laser (left of Figure 7), with velocity depicted by the blue arrows, resulting from the momentum transfer imparted by the Raman laser alone. For the concurrent mode of operation, the atom cloud enters one side of the chamber with a non-zero velocity perpendicular to the Raman laser (green arrow in Figure 7), for example, $v_{\text{cloud}} = 2.5 \text{ cm/s}$ (Carraz et al. 2014; Trimeche et al. 2019). An additional recoil laser with an axis perpendicular to the Raman laser imparts the transverse velocity v_{cloud} to the atom cloud. The first $\pi/2$ pulse is done on one side of the chamber by the first Raman laser, the π pulse is done by a second Raman laser in the middle of the chamber, and the third Raman laser on the opposite side of the chamber is responsible for the second $\pi/2$ pulse.

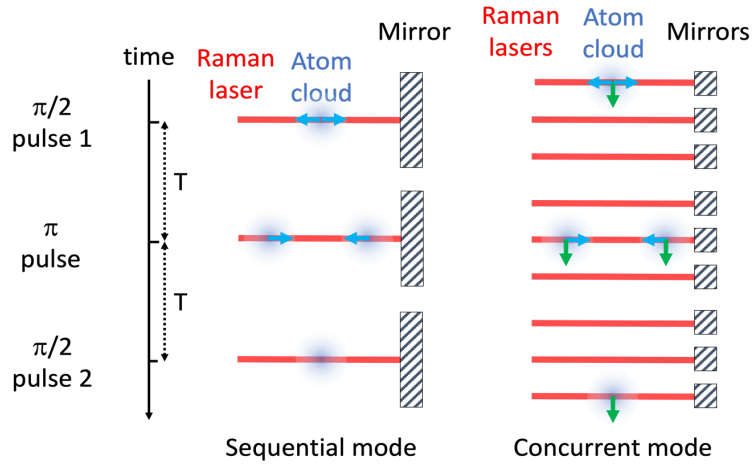


Figure 7: Diagram of the interferometry scheme for the sequential (left) and concurrent modes (right), showing the velocity of the wave-packets after the respective Raman laser pulses, which add momentum as represented by the blue arrows. In the case of the concurrent mode (right), the transverse velocity represented by the green arrow is provided at the start of the measurement sequence by an additional laser (not shown) perpendicular to the Raman lasers.

For both operation models, the mirror(s) tilt to compensate for the satellite rotation, i.e., they rotate between the laser pulses of the cold atom interferometer. The concurrent mode requires three mirrors in different locations along the direction of the atom movement.

2.4 Gradiometry

In both classic and quantum gravity gradiometry, we consider this technique to be implemented by combining pairs of accelerometers. As such, the error spectra of the

electrostatic and quantum accelerometers can be directly converted to gradiometer measurements by dividing the former by the length of the gradiometer arm L_{GG} , which is the distance between pairs of accelerometers in the same axis. Therefore, considering the MicroSTAR accelerometer (Section 2.3.1.2), with a noise floor of $2 \times 10^{-12} \text{ m/s}^2$, a gradiometer built with these instruments with $L_{GG} = 0.5\text{m}$ would have a noise floor of $4 \times 10^{-12} \text{ s}^{-2}$ or 4 mE.

The motivation for including a gradiometer in this study is to establish the requirements for a CAI gradiometer, considering that electrostatic accelerometers are unable to attain the necessary accuracy, as depicted in Figure 8. In this figure, the gravity gradient signal in the direction due to the time-variable gravity field, i.e. excluding the mean gravity field, at altitudes of 200 km and 300 km is shown in the yellow and red lines, respectively; the noise of GOCE gravity gradients is shown for reference in the blue line. Sub-mE gradiometry is required, which would need an electrostatic instrument that is at least one order of magnitude more accurate than the MicroSTAR accelerometer operating in ideal conditions.

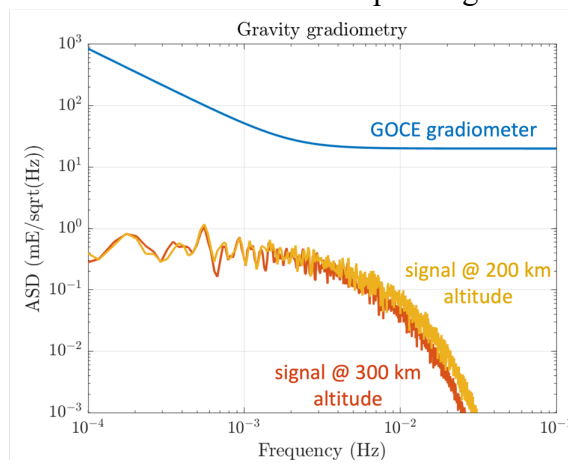


Figure 8: Comparison between the GOCE gradiometer errors (blue line) with the time-variable signal in terms of gravity gradient at 200 km (yellow line) and 300 km altitudes (red lines).

For quantum gradiometry, the measurement concept is similar to quantum accelerometry (Section 2.3.2), except that it is doubled along the axis where the gravity gradient is measured. The original atom cloud is physically split in two with a high recoil laser pulse, originating two CAI accelerometers. Differential acceleration is therefore measured between the 2 CAI accelerometers. Common acceleration is then rejected as the 2 CAI share the same Raman laser pulses and the gravity gradient along the Raman axis remains. This scheme applies to both sequential and concurrent modes of operation, with the obvious difference that the atom clouds will not be moving perpendicularly to the Raman laser in the first mode. The amplitude of the gravity gradient as a function of the differential phase measurement and associated errors is closely related to ϕ in Equation (15) and $\sigma_{CAI,ng}$ in Equation (20), as discussed in Section 3.2.2.

3 Measurement concepts and noise modelling

We consider two measurement concepts: low-low satellite-to-satellite tracking (ll-SST) and gravity gradiometry. We discuss the most beneficial configurations when using electrostatic and quantum instrumentation for both measurement concepts. For all cases, we derive the product noise spectra as a function of the instrument noise spectra, which were defined in Section 2.

In the following, vector equations are transformed into their components using indexes i, j and k for the coordinate axes x, y and z . Their relation is as arbitrary as the definition of the reference frames. For example, we may define $i, j, k \equiv x, y, z$ for along-track ll-SST and

$i, j, k \equiv y, z, x$ for cross-track II-SST, assuming the traditional axis nomenclature of x being aligned with the along-track direction, y with the cross-track direction and z with the radial direction, in a circular low-Earth orbit (LEO) orbit.

3.1 II-SST

The II-SST concept relies on precise ranging between two satellites flying in the same low-altitude orbit, separated by a certain distance along the orbit (220 km in the case of the GRACE and GRACE-FO missions). In a variant of this concept, labelled cross-track II-SST, the along-track distance is kept minimal, and the second orbit has a different right ascension of the ascending node than the first orbit to achieve ranging predominantly in the cross-track acceleration, away from the poles. The cross-track II-SST has to respect a minimum along-track separation for collision avoidance at the poles, where the orbit crosses each other. In all II-SST cases, the changes in the inter-satellite distance are caused by variations in gravity and non-gravitational forces. Therefore, the concept foresees accelerometers to measure the non-gravitational accelerations so that the signal due to gravity can be extracted from the ranging measurements.

3.1.1 II-SST with electrostatic accelerometers

The proposed II-SST concept is illustrated in Figure 9. The ISR system is similar to GRACE-FO's LRI, which is implemented in the so-called racetrack configuration with a triple mirror assembly (TMA). This concept has the benefit that the ISR is performed between the satellites' centres of mass without physically occupying those locations while not compromising the ranging performance (Sheard et al. 2012). In the case of electrostatic instrumentation, we foresee two accelerometers, labelled ACC 1 and ACC 2, symmetrically placed around the satellite centre of mass (CoM). This arrangement has the benefit that the accelerometers are sensitive to accelerations due to centrifugal and Euler forces and gravity gradients, which facilitates an accurate calibration of the accelerometers that would not be possible in the case of a single accelerometer placed into the satellite CoM. Although GRACE and GRACE-FO, at least for a part of their missions, operated successfully with only one accelerometer, the calibration process has always been problematic and requires parametrisation strategies that are usually derived empirically (Teixeira da Encarnação et al. 2020). We assume that the two accelerometers are at the nominal distance of $L_{acc} = 0.5$ m from each other.

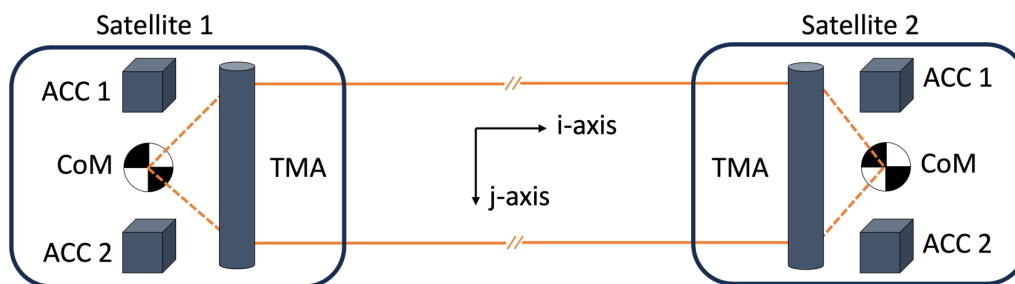


Figure 9: Diagram of the assumed concept for II-SST with electrostatic accelerometers.

The LRI is equipped with a DWS sensor that measures the direction of the incoming laser beam. Combined with accurate knowledge of the positions of the satellites from GNSS, this allows for deriving the attitude of the satellites relative to the Line-of-Sight (LOS) vector (Section 2.1.3.2). Obviously, this provides pitch and yaw, but not the roll about the LOS. The attitude is also observed by star trackers (Section 2.1.1), augmented by the accelerometers (Section 2.1.4), and optionally, a high-performance IMU (Section 2.1.2).

To extract the non-gravitational acceleration from the measurements of the accelerometers, we form the so-called common-mode acceleration (Massotti et al. 2021). The common mode acceleration along the generic axis i is:

$$a_{ng,i} = \frac{a_{1i} + a_{2i}}{2}, \quad (21)$$

where $i \equiv x$ is for the along-track ISR, and $i \equiv y$ is for the cross-track ISR. Through error propagation, we obtain the associated noise spectrum as a function of the linear acceleration error measured by a single accelerometer $\sigma_{acc,ng}(f)$ (Section 2.3.1):

$$\sigma_{ng}^2(f) = \frac{1}{2} \sigma_{acc,ng}^2(f). \quad (22)$$

The inter-satellite range acceleration $\ddot{\rho}$ still contains the effects of non-gravitational accelerations acting on the two satellites, which we remove by subtracting the common-mode accelerations, assuming that the i -axis is aligned with the LRI axis:

$$\ddot{\rho}_{grav} = \ddot{\rho} - a_{ng,i}^{(1)} + a_{ng,i}^{(2)}. \quad (23)$$

Error propagation gives the noise spectrum of $\ddot{\rho}_{grav}$ as a function of σ_{ng} and the ISR ranging error σ_{ISR} (Section 2.2):

$$\sigma_{\ddot{\rho}}^2(f) = \sigma_{ISR}^2(f) + 2\sigma_{ng}^2(f). \quad (24)$$

3.1.2 II-SST with quantum accelerometers

The II-SST concept is limited by the performance of the electrostatic accelerometers at longer wavelengths (frequencies near and below the orbital period), which motivates replacing them with quantum accelerometers to eliminate this limitation (Nicklaus et al. 2019). Contrary to the electrostatic accelerometers, the quantum ones do not need to be calibrated. Therefore, it is sufficient to place one quantum accelerometer into the satellite centre of mass, as shown in Figure 10, which has the benefit that the accelerometer directly measures the non-gravitational acceleration and is insensitive to centrifugal and Euler forces and gravity gradients. However, depending on the operational mode (Section 2.3.2.1), the atom cloud may be moving during the interferometric measurement process, and we need to account for the effects of the Coriolis force (Section 3.1.2.2).

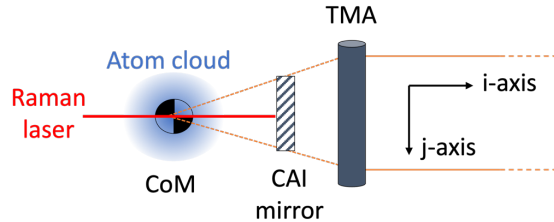


Figure 10: Diagram with the assumed concept of II-SST with quantum accelerometers. Only one satellite is shown.

The quantum accelerometer measures the phase Φ of the CAI, which is proportional to the acceleration of the atom cloud \mathbf{a}_{cloud} relative to the acceleration of the mirror that reflects the laser \mathbf{a}_{mirror} and the square of interrogation time T between laser pulses:

$$\Phi = \mathbf{k}_{eff} \cdot (\mathbf{a}_{cloud} - \mathbf{a}_{mirror})T^2, \quad (25)$$

where \mathbf{k}_{eff} is the effective wavevector that defines the direction in which the acceleration is sensed, and its magnitude is given by Equation (16).

Since the mirror is firmly attached to the satellite, it serves as a reference for the non-gravitational accelerations \mathbf{a}_{ng} experienced by the satellite so that:

$$\mathbf{a}_{mirror} = \mathbf{a}_{ng}. \quad (26)$$

In contrast, the atom cloud freely floated in inertial space during the interrogation time. The acceleration of the atom cloud can be expressed as:

$$\mathbf{a}_{\text{cloud}} = -(\mathbf{V} - \boldsymbol{\Omega}^2 - \dot{\boldsymbol{\Omega}})(\mathbf{r}_{\text{cloud}} - \mathbf{r}_{\text{CoM}}) + 2\boldsymbol{\omega} \times \mathbf{v}_{\text{cloud}}, \quad (27)$$

with the gravity gradient tensor as:

$$\mathbf{V} = \begin{bmatrix} V_{ii} & V_{ij} & V_{ik} \\ V_{ij} & V_{jj} & V_{jk} \\ V_{ik} & V_{jk} & V_{kk} \end{bmatrix}, \quad (28)$$

the angular velocity vector as:

$$\boldsymbol{\omega} = \begin{bmatrix} \omega_i \\ \omega_j \\ \omega_k \end{bmatrix},$$

the angular rate tensor as:

$$\boldsymbol{\Omega} = \begin{bmatrix} 0 & -\omega_k & \omega_j \\ \omega_k & 0 & -\omega_i \\ -\omega_j & \omega_i & 0 \end{bmatrix} \text{ and } \boldsymbol{\Omega}^2 = \begin{bmatrix} -\omega_j^2 - \omega_k^2 & \omega_i\omega_j & \omega_i\omega_k \\ \omega_i\omega_j & -\omega_k^2 - \omega_i^2 & \omega_j\omega_k \\ \omega_i\omega_k & \omega_j\omega_k & -\omega_i^2 - \omega_j^2 \end{bmatrix} \quad (29)$$

and the angular acceleration as:

$$\dot{\boldsymbol{\Omega}} = \begin{bmatrix} 0 & -\dot{\omega}_k & \dot{\omega}_j \\ \dot{\omega}_k & 0 & -\dot{\omega}_i \\ -\dot{\omega}_j & \dot{\omega}_i & 0 \end{bmatrix}. \quad (30)$$

The remaining symbols are the position of the atom cloud $\mathbf{r}_{\text{cloud}}$, position of the satellite CoM \mathbf{r}_{CoM} , and the velocity of the atom cloud $\mathbf{v}_{\text{cloud}}$ relative to the satellite centre of mass. The term $\dot{\boldsymbol{\Omega}}$ represents the angular acceleration matrix which causes Euler accelerations, $\boldsymbol{\Omega}^2$ causes the centrifugal accelerations, and $2\boldsymbol{\omega} \times \mathbf{v}_{\text{cloud}}$ is the Coriolis acceleration.

It should be noted that $\boldsymbol{\Omega}$ is the angular velocity after any compensation by a tilting mirror, which also minimises the loss of contrast of the cold atom interferometer (Trimeche et al. 2019).

Combining the above, we obtain the measured acceleration along the direction defined by the Raman laser axis, represented by the unit vector $\mathbf{e}_i = \mathbf{k}_{\text{eff}}/k_{\text{eff}}$, as:

$$\begin{aligned} \mathbf{e}_i \cdot \mathbf{a}_{\text{ng}} &= \\ &= -\frac{\Phi}{k_{\text{eff}}T^2} + \mathbf{e}_i \cdot \left(-(\mathbf{V} - \boldsymbol{\Omega}^2 - \dot{\boldsymbol{\Omega}})(\mathbf{r}_{\text{cloud}} - \mathbf{r}_{\text{CoM}}) + 2\boldsymbol{\omega} \times \mathbf{v}_{\text{cloud}} \right). \end{aligned} \quad (31)$$

The derivation of the equation above can be found in Section 8.1.1.

Since we measure the acceleration in the direction of the wavevector \mathbf{k}_{eff} , this vector must be aligned with the laser used for measuring the inter-satellite range. Further, we ignore any effects of magnetic fields and self-gravity on the atom cloud, which might play a role in view of the extreme sensitivity of the quantum sensor. These considerations are beyond the scope of this study because they heavily depend on the specific instrument and satellite design.

If the atom cloud is in the satellite centre of mass, i.e., $\mathbf{r}_{\text{cloud}} - \mathbf{r}_{\text{CoM}} = \mathbf{0}$, the equation above simplifies to:

$$\mathbf{e}_i \cdot \mathbf{a}_{\text{ng}} = -\frac{\Phi}{k_{\text{eff}}T^2} + \mathbf{e}_i \cdot (2\boldsymbol{\omega} \times \mathbf{v}_{\text{cloud}}), \quad (32)$$

leaving the Coriolis term as the only effect to consider. In this context, we note that $\mathbf{r}_{\text{cloud}} - \mathbf{r}_{\text{CoM}} = \mathbf{0}$ holds for the initial atom cloud position. The first laser pulse of the cold atom interferometer splits the wave-packet in two that move at a similar speed in opposite directions along the laser axis away from the initial position, indicated as step ii in Section 2.3.2. We assume that the rate of rotation of the Raman laser, i.e., the rotation of the satellite after the compensation by the tilting mirror, does not change significantly during the outward

and inward wave-packet drift, indicated as steps ii to iv in Section 2.3.2. Under these conditions, the integrated effect of the rotational and gravity gradient terms cancel out over the outward and inward motion of the two wave-packets and are negligible at their recombination.

Considering axis i, j and k are arbitrary, e.g., $i, j, k \equiv x, y, z$ for along-track II-SST and $i, j, k \equiv y, z, x$ for cross-track II-SST, we can express the equation in scalar form as:

$$a_{\text{ng},i} = -\frac{\Phi}{k_{\text{eff}}T^2} + 2\omega_j v_{\text{cloud},k} - 2\omega_k v_{\text{cloud},j}. \quad (33)$$

3.1.2.1 Error amplitude of quantum accelerometers

Considering the error in the atom cloud velocity knowledge $\sigma_{v,\text{cloud}}$, angular rate error σ_ω after compensation by the tilting mirror, and applying error propagation, we obtain:

$$\begin{aligned} \sigma_{a_{\text{ng},i}}^2 &= \frac{\sigma_\Phi^2}{k_{\text{eff}}^2 T^4} + \\ &+ 4\omega_j^2 \sigma_{v,\text{cloud},k}^2 + 4\omega_k^2 \sigma_{v,\text{cloud},j}^2 + 4\sigma_{\omega,j}^2 v_{\text{cloud},k}^2 + 4\sigma_{\omega,k}^2 v_{\text{cloud},j}^2. \end{aligned} \quad (34)$$

We can group the first term as the CAI acceleration sensitivity error $\sigma_{\text{CAI,ng}}$ (cf. Section 2.3.2) and the last four terms as the errors $\sigma_{\text{Cor},i}$ caused by the Coriolis effect:

$$s_{a_{\text{ng},i}}^2 \equiv \sigma_{\text{CAI,ng}}^2 + \sigma_{\text{Cor},i}^2. \quad (35)$$

For the conservative case that errors, cloud velocities and angular rates are homogeneous in any direction, the errors resulting from Coriolis acceleration $\sigma_{\text{Cor},i}$ is:

$$\sigma_{\text{Cor},i}^2 = 8\omega^2 \sigma_{v,\text{cloud}}^2 + 8\sigma_\omega^2 v_{\text{cloud}}^2. \quad (36)$$

3.1.2.2 Amplitude of the Coriolis term

The equation of the variance of the Coriolis term depends on the velocity of the atom cloud and the angular velocity of the Raman laser, cf. Equation (36). In this section, we analyse the individual contributions in more detail and explain the underlying assumptions on signals and errors.

3.1.2.2.1 Cloud velocity

The atom cloud velocity components that contribute to the variance of the Coriolis term are perpendicular to the Raman laser axis since we assume that the integrated effects from the outwards and inwards movement of the cloud along the Raman laser axis are negligible. Since no instrument is perfect, the atom cloud will have a random non-zero velocity when released from the MOT. We assume the worst-case value of the initial cloud velocity to be $\sigma_{v_{\text{cloud,initial}}} = 10^{-7}$ m/s. It should be noted that treating this worst-case value as an error is a conservative estimate.

The thermal velocity (most probable speed) of individual atoms is:

$$v_{\text{atom,therm}} = \sqrt{\frac{2k_B T_{\text{atom}}}{m}}, \quad (37)$$

where k_B is the Stefan Boltzmann constant, T_{atom} is the atom temperature, and m is the atom mass. In practice, $v_{\text{atom,therm}}$ tends to be at the order of 10^{-4} m/s, but a technique called Delta Kick-Collimation (DKC) allows for values at the micrometre per second (Amri, 2022). For this reason, we assume that $v_{\text{atom,therm}} = 10^{-6}$ m/s.

Recalling that the velocity dispersion follows the Maxwell-Boltzmann distribution (Amri, 2022), we are interested in the difference between the most probable speed $v_{\text{atom,therm}}$ and the

velocity RMS, which is given by $\sqrt{3/2}v_{\text{atom,therm}}$. Under this assumption, the thermal velocity of the atom cloud is:

$$\sigma_{v_{\text{cloud,therm}}} = \frac{\left(\sqrt{\frac{3}{2}} - 1\right)v_{\text{atom,therm}}}{\sqrt{N}}, \quad (38)$$

due to the averaging over N atoms. Thus, assuming that $\sigma_{v_{\text{cloud,initial}}}$ is uncorrelated to $\sigma_{v_{\text{cloud,therm}}}$, the variability of the atom cloud velocity is:

$$\sigma_{v_{\text{cloud}}}^2 = \sigma_{v_{\text{cloud,therm}}}^2 + \sigma_{v_{\text{cloud,initial}}}^2. \quad (39)$$

3.1.2.2.2 Angular velocity

We remind that the angular velocity ω_i is not necessarily the satellite angular velocity but the residual angular velocity after compensation by the tilting mirror if the mission concepts under analysis assume this capability. To make this distinction, we introduce the symbol $\delta\omega$ when relevant but derive all equations with the original symbol for angular velocity ω .

The mean angular velocity of a nadir-pointing satellite in low-Earth orbit is the pitch rate of about $\omega_y = 1.1 \times 10^{-3}$ rad/s, with the y -axis aligned with the cross-track direction. The yaw and roll rate are typically at least one order of magnitude smaller, i.e., about $\omega_x = \omega_z = 1 \times 10^{-4}$ rad/s, with the x -axis aligned with the along-track direction and the z -axis right-hand orthogonal (which is parallel to the radial direction in a circular orbit).

The compensation of the angular velocity requires that either the satellite attitude or the tilting mirrors are controlled, taking input from a sensor that provides angular velocity measurements. One of the best-performing angular velocity sensors is the Astrix 200 laser gyroscope, which has an accuracy of $\sigma_\omega = 5 \times 10^{-8}$ rad/s. We believe that it will not be possible to fully exploit the gyroscope's performance in real-time and assume an accuracy degradation given by the factor f_ω :

$$\delta\omega = f_\omega \sigma_\omega, \quad (40)$$

taken to be one order of magnitude, $f_\omega = 10$, worse than the measurement system, i.e., $\delta\omega = 5 \times 10^{-7}$ rad/s for the case of the mirror compensating the satellite rotation driven by the Astrix 200 gyroscope. When the satellite rotation is compensated in this way, we assume $\omega = \delta\omega$. In addition to avoiding loss of contrast in the cold atom interferometer, these figures already suggest that the compensation of the satellite rotation is necessary for quantum accelerometers, depending on the sensitivity to the Coriolis effect, to be quantified in Section 5.1.

We only consider attitude compensation for the cases of quantum accelerometry or gradiometry. We do not consider this for electrostatic accelerometers or classic gradiometers, for example, by physically rotating the instrument within the satellite body.

3.2 Gradiometry

The only distinction between classic and quantum gradiometry is that in the case of the former, the accelerometers are sensitive to all directions, which results in the possibility of measuring off-diagonal gravity gradient components, even with a single gradiometer arm. In the case of quantum gravimetry, the CAI instruments we consider are inherently unidirectional and only sensitive to the gravity gradient along the axis connecting the atom clouds. Three CAI gradiometer instruments installed perpendicular to each other in the same satellite are needed to retrieve all diagonal terms of the gravity gradient tensor. For simplicity, we assume this to be the case without going into more detail regarding the engineering aspects of this configuration. For more details of the configuration, the reader is invited to read Trimeche et al. (2019).

3.2.1 Gradiometry with electrostatic accelerometers

The GOCE mission demonstrated gravity gradiometry based on electrostatic accelerometers. The configuration of accelerometers is illustrated in Figure 11. Here, we assume the same concept but with more advanced accelerometers and, potentially, a high-performance gyroscope. For reference, we will assume a distance of $L_{GG} = 0.5$ m between the accelerometers located on the same axis.

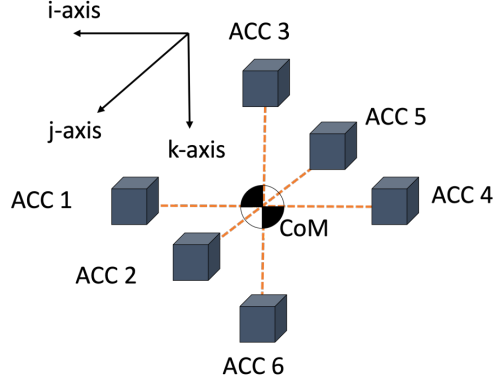


Figure 11: Accelerometer configuration in the classic gravity gradiometry concept.

3.2.1.1 Error amplitude of classic gradiometers

The diagonal element V_{ii} of the gravity gradient tensor, measured by the accelerometer pair 1 and 4, is calculated by (Rummel, Yi, and Stummer 2011):

$$V_{ii} = -\frac{a_{1,i} - a_{4,i}}{L_{GG}} - \omega_j^2 - \omega_k^2. \quad (41)$$

For the remaining diagonal elements V_{jj} and V_{kk} , the expressions are similar with accelerometers pairs 2,5 and 3,6, respectively, and angular velocity components i,k and i,j , respectively. After error propagation, there will be non-linear terms that result in the product of angular velocity and angular velocity noise components, following approximations such as:

$$(\omega_i + \sigma_{\omega,i})^2 \approx \omega_i^2 + 2\omega_i\sigma_{\omega,i}. \quad (42)$$

This relation illustrates the coupling between the angular velocity signal ω_i and the angular velocity noise $\sigma_{\omega,i}$, along the generic axis i .

The errors associated with classic gradiometry are:

$$\sigma_{V_{ii}}^2(f) = \frac{2}{L_{GG}^2} \sigma_{acc,ng}^2(f) + 4 \left((\text{RMS}(\omega_j))^2 + (\text{RMS}(\omega_k))^2 \right) \sigma_{\omega}^2(f), \quad (43)$$

where $\text{RMS}(\omega_j)$ and $\text{RMS}(\omega_k)$ are the RMS of the angular velocity signal, which signifies the coupling between signal and noise in the non-linear error propagation. For the pitch rate, we assume $\text{RMS}(\omega_y) \approx 1.1 \times 10^{-3} \text{ rad/s}$ and for the yaw and roll rate, $\text{RMS}(\omega_x) \approx \text{RMS}(\omega_z) \approx 10^{-4} \text{ rad/s}$. The underlying assumptions for deriving these RMS values are explained in Appendix 8.1. For the remaining diagonal terms, the corresponding expressions are similar to Equation (43), considering the RMS of the orthogonal angular velocity components.

The off-diagonal elements of the gravity gradient tensor are given by:

$$\begin{aligned} V_{ij} &= -\frac{a_{2,i} - a_{5,i}}{2L_{GG}} - \frac{a_{1,j} - a_{4,j}}{2L_{GG}} + \omega_i\omega_j \\ V_{ik} &= -\frac{a_{1,k} - a_{4,k}}{2L_{GG}} - \frac{a_{3,i} - a_{6,i}}{2L_{GG}} + \omega_i\omega_k \end{aligned} \quad (44)$$

$$V_{jk} = -\frac{a_{3,j} - a_{6,j}}{2L_{GG}} - \frac{a_{2,k} - a_{5,k}}{2L_{GG}} + \omega_j \omega_k$$

Applying error propagation results in:

$$\sigma_{V_{ij}}^2(f) = \frac{1}{L_{GG}^2} \sigma_{acc,ng}^2(f) + \left((\text{RMS}(\omega_i))^2 + (\text{RMS}(\omega_j))^2 \right) \sigma_{\omega}^2(f). \quad (45)$$

The expressions for the remaining off-diagonal components are similar, with the RMS of the angular velocity components ω_i , ω_k and ω_j , ω_k relevant to the tensor component ik and jk , respectively.

3.2.1.2 Attitude reconstruction with classic gradiometers

We analyse the capability of the classic gradiometer to measure angular acceleration and separate gravity gradients from frame rotations. It is fair to assume that the satellite will be equipped with star sensors attitude reconstruction, both on board as well as in-ground processing. We assume the errors of this instrument are given by Equation (3).

The gravity gradiometer also functions by design as an accurate angular acceleration sensor, from which the angular velocity can be obtained by numerical integration. The noise ASD of the gradiometer-derived angular accelerations are derived from the accelerometer measurements as follows:

$$\begin{aligned} \dot{\omega}_i &= \frac{a_{2,k} - a_{5,k}}{2L_{GG}} - \frac{a_{3,j} - a_{6,j}}{2L_{GG}}, \\ \dot{\omega}_j &= \frac{a_{3,i} - a_{6,i}}{2L_{GG}} - \frac{a_{1,k} - a_{4,k}}{2L_{GG}}, \\ \dot{\omega}_k &= \frac{a_{1,j} - a_{4,j}}{2L_{GG}} - \frac{a_{2,i} - a_{5,i}}{2L_{GG}}. \end{aligned} \quad (46)$$

Since all accelerometer axes have the same performance, we find:

$$\sigma_{\dot{\omega},GG}(f) = \frac{1}{L_{GG}} \sigma_{acc,ng}(f), \quad (47)$$

for the noise ASD of the gradiometer-derived angular acceleration measurements, where $\sigma_{acc,ng}(f)$ is the noise ASD of a linear acceleration measurement of an individual accelerometer. It is worthwhile to note that the angular acceleration measurements derived in this way are more accurate than the angular acceleration measurements of the individual accelerometers as illustrated in Figure 12, taking MicroSTAR (Section 2.3.1.2) as an example.

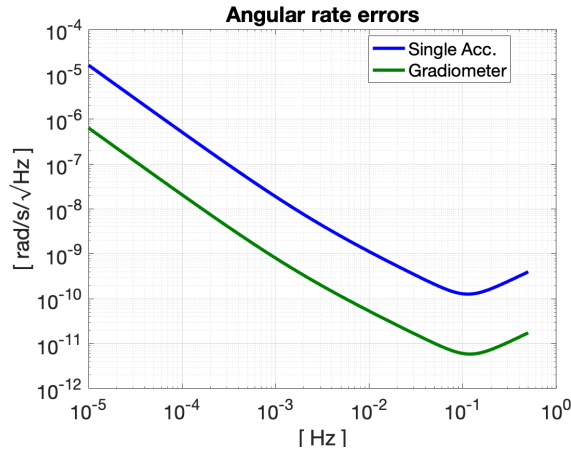


Figure 12: Noise spectra of the angular velocity derived from the linear acceleration measurements of two accelerometers installed in a gradiometer arm with length $L_{GG} = 0.5$ m (green line) and of the angular acceleration measurements of a single accelerometer (blue line).

The discrepancy between the attitude accuracies in Figure 12 can be explained by the small distance (a few cm) between the electrodes for the single accelerometer and the larger gradiometer arm (50 cm) separating the accelerometers.

3.2.2 Gradiometry with Quantum Sensors

Gravity gradiometry based on quantum sensors relies on generating an initial cloud of atoms that is physically split into two atom clouds, labelled “Cloud 1” and “Cloud 2” in Figure 13. The advantage is that the relative cloud positions are well-known because the splitting is performed by a laser pulse that gives an accurately known kick to the initial cloud of atoms. Once the two atom clouds are in position, the cold atom interferometric sequence starts for both atom clouds simultaneously using the same Raman laser. In principle, it is the same sequence of laser pulses as for quantum accelerometers. Thus, the quantum gradiometer is also based on sensing the differential acceleration along the laser axis over the precisely known distance between the atom clouds. Consequently, the equations presented in Section 2.3.2 also apply to quantum gravity gradiometry.

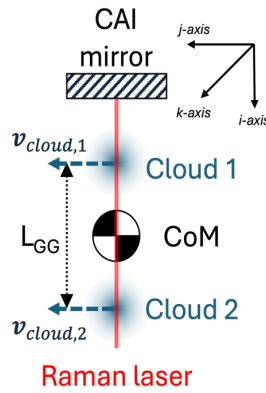


Figure 13: Quantum gravity gradiometer concept.

By re-arranging Equation (31), we find:

$$\frac{\Phi_{i,l}}{k_{\text{eff}}T^2} = \mathbf{e}_i \cdot \left(-\mathbf{a}_{\text{ng},l} - (V - \Omega^2 - \dot{\Omega})(\mathbf{r}_{\text{cloud},l} - \mathbf{r}_{\text{CoM}}) + 2\boldsymbol{\omega} \times \mathbf{v}_{\text{cloud},l} \right), \quad (48)$$

where $l = 1$ or 2 identifies the atom cloud (cf. Figure 13). Setting the origin of the reference axis at the CoM, the atom clouds are at the positions $\mathbf{r}_{\text{cloud},1} = -\mathbf{r}_{\text{cloud},2} \equiv L_{\text{GG}}/2\mathbf{e}_i$ at the time the interferometry is done.

Regarding the cloud velocity, we have $\mathbf{v}_{\text{cloud},1} = \mathbf{v}_{\text{cloud},2}$ and:

$$\mathbf{v}_{\text{cloud},l} = \mathbf{v}_{\text{cloud,therm},l} + \mathbf{v}_{\text{cloud,initial},l} = \mathbf{v}_{\text{cloud,therm},l} + v_{\text{cloud,initial},l} \cdot \mathbf{e}_j. \quad (49)$$

In the case of the concurrent mode of operation (Section 2.3.2.1), $\mathbf{v}_{\text{cloud,initial},l}$ reflects the transverse velocity imparted by an additional laser perpendicular to the Raman laser axis. In this case, we note that $v_{\text{cloud,initial},1} = v_{\text{cloud,initial},2}$ because both clouds are accelerated with the same recoil laser (not shown in Figure 13). In the case of the sequential mode, $v_{\text{cloud,initial},1} = v_{\text{cloud,initial},2} = 0$. In both cases, $\mathbf{a}_{\text{ng},1} = \mathbf{a}_{\text{ng},2}$ because the non-gravitational accelerations affect both clouds equally. As a result, these two terms cancel when computing the differential measurement $\delta\Phi_i \equiv \Phi_{i,1} - \Phi_{i,2}$:

$$\frac{\delta\Phi_i}{k_{\text{eff}}T^2} = \mathbf{e}_i \cdot \left(-(V - \Omega^2 - \dot{\Omega})L_{\text{GG}}\mathbf{e}_i + 2\boldsymbol{\omega} \times \mathbf{v}_{\text{cloud,therm}} \right), \quad (50)$$

The term on $\mathbf{v}_{\text{cloud,therm},l}$ does not cancel because it is related to the thermal velocity of the cloud, which is akin to a random variable.

Recognising that $\dot{\boldsymbol{\Omega}}\mathbf{e}_i = \dot{\boldsymbol{\Omega}}\mathbf{e}_j = \dot{\boldsymbol{\Omega}}\mathbf{e}_k = 0$ (cf. Equation (30)), isolating the gravity gradient term, and reducing the vector equation to a scalar quantity results in:

$$V_{ii} = -\frac{1}{L_{GG}} \frac{\delta\Phi_i}{k_{eff}T^2} - \omega_j^2 - \omega_k^2 + \frac{2}{L_{GG}} (\omega_j v_{\text{cloud,therm},k} - \omega_k v_{\text{cloud,therm},j}). \quad (51)$$

The derivation of the equation above and the one for other axes is in Appendix 8.1.2. As a side note, if we assume a quantum gravity gradiometer concept where the satellite rotation is compensated by a tilting mirror, as described in Section 3.1.2, the symbol ω should be interpreted as the compensated attitude $\delta\omega$, given by Equation (40).

3.2.2.1 Error amplitude of quantum gradiometers

Applying error propagating to Equation (50), under the assumption that Raman laser is rotating at the residual angular velocity after compensation by the tilting mirror $\delta\omega$, and considering uncorrelated phase errors, $\sigma_{\delta\Phi_i}^2 = \sigma_{\Phi_{i,1}}^2 + \sigma_{\Phi_{i,2}}^2 = 2\sigma_{\Phi}^2$, results in the errors associated with quantum gradiometry:

$$\begin{aligned} \sigma_{V_{ii}}^2 &= \frac{2}{L_{GG}^2} \frac{\sigma_{\Phi_i}^2}{k_{eff}^2 T^4} + 4\omega_j^2 \sigma_{\omega_j}^2 + 4\omega_k^2 \sigma_{\omega_k}^2 \\ &+ \frac{16}{L_{GG}^2} (\omega_j^2 \sigma_{v_{\text{cloud,therm},k}}^2 + \omega_k^2 \sigma_{v_{\text{cloud,therm},j}}^2 + \\ &\sigma_{\omega,j}^2 v_{\text{cloud,therm},k}^2 + \sigma_{\omega,k}^2 v_{\text{cloud,therm},j}^2). \end{aligned} \quad (52)$$

Under the conservative assumption of homogeneous noise in all components:

$$\begin{aligned} \sigma_V^2 &= \frac{2}{L_{GG}^2} \frac{\sigma_{\Phi}^2}{k_{eff}^2 T^4} + 8\omega^2 \sigma_{\omega}^2 + \frac{32}{L_{GG}^2} (\omega^2 \sigma_{v_{\text{cloud,therm}}}^2 + \sigma_{\omega}^2 v_{\text{cloud,therm}}^2) \\ &\equiv \sigma_{V_{\text{CAI}}}^2 + \sigma_{\Omega^2}^2 + \sigma_{V_{\text{Cor}}}^2 = \frac{2}{L_{GG}^2} \sigma_{\text{CAI,ng}}^2 + \sigma_{\Omega^2}^2 + \frac{4}{L_{GG}^2} \sigma_{\text{Cor}}^2, \end{aligned} \quad (53)$$

with expressions for $\sigma_{\text{CAI,ng}}$ and σ_{Cor}^2 given in Section 3.1.2.1, and the errors associated with the centrifugal accelerations are $\sigma_{\Omega^2} = \sqrt{8}\omega\sigma_{\omega}$.

3.2.2.2 Attitude reconstruction with quantum gradiometers

In the case of classic gradiometry (Section 3.2.1), the 6 capacitive accelerometers that compose the 3D gradiometer make it possible to estimate the rate of change of the attitude (Section 3.2.1.2). For CAI gradiometry, the case is not the same since the ‘‘accelerometers’’ are unidimensional. This section explores how single-axis quantum gradiometers can be arranged so that they also provide complete attitude information.

Consider the m -th CAI gradiometer aligned with the i -axis (parallel to \mathbf{e}_i), shown in Figure 14.

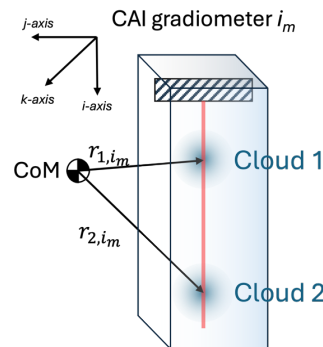


Figure 14: CAI gradiometer m , aligned with axis i , showing the positions of the atom clouds 1 and 2. From Equation (27), with the reference frame at the CoM, the phase measurement Φ_{l,i_m} of the atom cloud l is:

$$\begin{aligned} \frac{\Phi_{l,i_m}}{k_{\text{eff}}T^2} &= \mathbf{e}_i \cdot \left(-(\mathbf{V} - \boldsymbol{\Omega}^2 - \dot{\boldsymbol{\Omega}})\mathbf{r}_{l,i_m} + 2\boldsymbol{\omega} \times \mathbf{v}_{\text{cloud}} \right) = \\ &\mathbf{e}_i \cdot \begin{bmatrix} -V_{ii} - \omega_j^2 - \omega_k^2 & -V_{ij} + \omega_i\omega_j - \dot{\omega}_k & -V_{ik} + \omega_i\omega_k + \dot{\omega}_j \\ -V_{ij} + \omega_i\omega_j + \dot{\omega}_k & -V_{jj} - \omega_i^2 - \omega_k^2 & -V_{jk} + \omega_j\omega_k - \dot{\omega}_i \\ -V_{ik} + \omega_i\omega_k - \dot{\omega}_j & -V_{jk} + \omega_j\omega_k + \dot{\omega}_i & -V_{kk} - \omega_i^2 - \omega_j^2 \end{bmatrix} \mathbf{r}_{l,i_m} + \\ &\mathbf{e}_i \cdot \begin{bmatrix} \omega_j v_{l,i_m,k} - \omega_k v_{l,i_m,j} \\ \omega_k v_{l,i_m,i} - \omega_i v_{l,i_m,k} \\ \omega_i v_{l,i_m,j} - \omega_j v_{l,i_m,i} \end{bmatrix} + \mathbf{e}_i \cdot \mathbf{a}_{\text{ng}}. \end{aligned} \quad (54)$$

Any linear combination of the two phase measurements Φ_{1,i_m} and Φ_{2,i_m} will unavoidably include off-diagonal terms of \mathbf{V} , $\boldsymbol{\Omega}^2$ and $\dot{\boldsymbol{\Omega}}$ because \mathbf{r}_{l,i_m} is not aligned with \mathbf{e}_i . Therefore, there will be 15 unknowns:

- 6 gravity gradients \mathbf{V} ,
- 3 angular rates $\boldsymbol{\omega}$ (or accelerations $\dot{\boldsymbol{\Omega}}$),
- 3 non-gravitational accelerations \mathbf{a}_{ng} and
- 3 Coriolis accelerations $\boldsymbol{\omega} \times \mathbf{v}_{\text{cloud}}$ (or atom cloud velocities $\mathbf{v}_{\text{cloud}}$).

In the case of the common and differential linear combinations, 3 degrees of freedom cancel out: the diagonal of the gravity gradient and the non-gravitational accelerations, respectively. In both cases, we are left with 12 unknowns, which require 12 CAI gradiometers to resolve fully.

One possible arrangement of CAI gradiometers is indicated in Figure 15 as a “ring” of 4 gradiometer arms arranged symmetrically around the CoM in the same plane, perpendicular to the k -axis and intersecting the CoM.

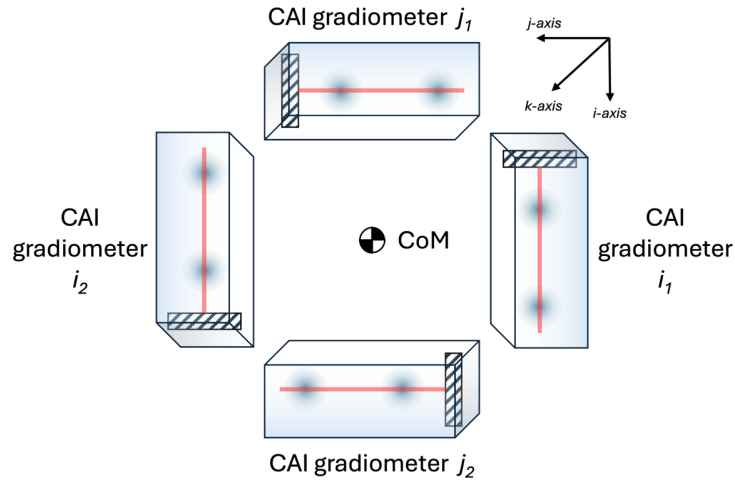


Figure 15: Arrangement of 4 CAI gradiometers placed symmetrically around the CoM that are able to measure $a_{\text{ng},i}$, $a_{\text{ng},j}$ and $\dot{\omega}_k$.

The common phase measurement $\sum \Phi_{i1}$ (or $\sum \Phi_{i2}$) and $\sum \Phi_{j1}$ (or $\sum \Phi_{j2}$) of gradiometer il (or $i2$) and jl (or $j2$) provides information on the i -th and j -th component of the non-gravitational accelerations, respectively. The difference between the common phases $\sum \Phi_{i1} - \sum \Phi_{i2}$ or $\sum \Phi_{j1} - \sum \Phi_{j2}$ cancels the Coriolis and non-gravitational accelerations. The sum of the difference of the common phases $\sum \Phi_{i1} - \sum \Phi_{i2} + \sum \Phi_{j1} - \sum \Phi_{j2}$ cancels the gravity gradients and centrifugal accelerations, isolating the $\dot{\omega}_k$ term and, consequently, ω_k by numerical integration. It should be noted that the complete attitude of the satellite could only be determined with the help of an absolute attitude sensor, such as a star tracker, to resolve the attitude bias and bias rate in the case of the proposed CAI gradiometer ring, resulting from the unknown integration constant.

If two orthogonal rings measure the k and j components of the angular acceleration, that would be sufficient to completely retrieve the measurement of the V_{ii} , which would ideally be aligned with the radial direction. This is because ω_i does not affect the measurement of V_{ii} . If a third orthogonal ring is added, then the complete diagonal of \mathbf{V} is available.

4 Effects of attitude uncertainty

So far, we derive the noise spectra for the observations in the satellite reference frame. However, the observations need to be transformed to the Earth-centred, Earth-fixed (ECEF) reference frame. The transformation requires satellite attitude data and is, therefore, not free of errors. In this section, we will analyse the impact of attitude errors.

The effects of attitude uncertainty discussed in this section are conceptually separate from other attitude errors discussed so far. This refers notably to the Coriolis effect on CAI accelerometers or gradiometers (Section 3.1.2.2) and the capability of gradiometers to observe attitude rates, analysed in Section 3.2.1.2 for the classical case, and in Section 3.2.2.2 for a collection of CAI gradiometers.

4.1 II-SST

Conceptually, we need to subtract the ISR acceleration $\ddot{\rho}_{ng}$ due to non-gravitational accelerations from the measured ISR acceleration $\ddot{\rho}$ to obtain the ISR $\ddot{\rho}_{grav}$ due to gravitational accelerations:

$$\ddot{\rho}_{grav} = \ddot{\rho} - \ddot{\rho}_{ng}. \quad (55)$$

The ISR acceleration $\ddot{\rho}_{ng}$ is the differential non-gravitational acceleration projected onto the line-of-sight connecting the two satellites' centres of mass, i.e.:

$$\ddot{\rho}_{ng} = (\mathbf{a}_{ng}^{(1)} - \mathbf{a}_{ng}^{(2)}) \cdot \mathbf{e}_{LOS} = \Delta \mathbf{a}_{ng} \cdot \mathbf{e}_{LOS}, \quad (56)$$

where \mathbf{e}_{LOS} is the line-of-sight unit vector and $\mathbf{a}_{ng}^{(1)}$ and $\mathbf{a}_{ng}^{(2)}$ are the measured non-gravitational accelerations of satellite 1 and satellite 2, respectively, all defined in the Earth-centred, inertial (ECI) reference. The line-of-sight is defined by the satellite positions, which are naturally provided in the ECI frame.

$$\mathbf{e}_{LOS} = \frac{\mathbf{r}^{(1)} - \mathbf{r}^{(2)}}{\|\mathbf{r}^{(1)} - \mathbf{r}^{(2)}\|}. \quad (57)$$

If $\mathbf{r}^{(1)}$ or $\mathbf{r}^{(2)}$ are provided in the ECEF frame, we assume that the coordinate transformations do not introduce a significant error because the Earth Orientation Parameters are well known. As for the non-gravitational accelerations, they are measured in the Satellite Reference Frame (SRF), which we represent $\mathbf{a}_{ng}^{(SRF,s)}$ for satellite s .

We need to perform a coordinate transformation for the accelerations, based on the satellite attitude data, from the Satellite Reference Frame (SRF) to the Earth-centred, inertial frame, which can be represented as

$$\mathbf{a}_{ng}^{(ECI,s)} = \mathbf{R}^{(ECI \leftarrow SRF,s)} \mathbf{a}_{ng}^{(SRF,s)}. \quad (58)$$

The SRF-to-ECI rotation matrix contains errors, here represented by the small angle rotation matrix $\Theta^{(ECI \leftarrow SRF,s)}$:

$$\mathbf{R}^{(ECI \leftarrow SRF,s)} = \mathbf{R}^{(ECI \leftarrow SRF,s,true)} \Theta^{(ECI \leftarrow SRF,s)}. \quad (59)$$

We split $\Theta^{(ECI \leftarrow SRF,s)}$ into the identity matrix and the small angle rotations, given as Euler angles errors $\theta_{roll,s}$, $\theta_{pitch,s}$ and $\theta_{yaw,s}$ for satellite s :

$$\mathbf{\Theta}^{(ECI \leftarrow SRF,s)} = \mathbf{E}^{(s)} + \mathbf{I} = \begin{bmatrix} 0 & -\theta_{yaw,s} & \theta_{pitch,s} \\ \theta_{yaw,s} & 0 & -\theta_{roll,s} \\ -\theta_{pitch,s} & \theta_{roll,s} & 0 \end{bmatrix} + \mathbf{I}. \quad (60)$$

With these definitions, we can write:

$$\mathbf{a}_{ng}^{(ECI,s)} = \mathbf{a}_{ng}^{(ECI,true,s)} + \mathbf{E}^{(s)} \mathbf{a}_{ng}^{(SRF,s)}, \quad (61)$$

where the only term on the right-hand side that is not perfectly known (for this analysis) is $\mathbf{E}^{(s)} \mathbf{a}_{ng}^{(SRF,s)}$. Replacing in Equation (51):

$$\ddot{\rho}_{ng}^{(ECI)} = \left(\Delta \mathbf{a}_{ng}^{(ECI,true)} + (\mathbf{E}^{(1)} - \mathbf{E}^{(2)}) \Delta \mathbf{a}_{ng}^{(SRF)} \right) \cdot \mathbf{e}_{LOS}^{(ECI)}, \quad (62)$$

Assuming the attitude errors of $\mathbf{E}^{(s)}$, represented by the vector $\boldsymbol{\sigma}_\theta$, are the same for both satellites, the error propagation of Equation (56), after replacing Equation (61), is

$$\sigma_{\dot{\rho}_{ng,\theta}}^{(ECI)} = \nabla \ddot{\rho}_{ng}^{(ECI)} [\boldsymbol{\sigma}_\theta] \nabla \ddot{\rho}_{ng}^{(ECI)T}, \quad (63)$$

with the Jacobian $\nabla = \left[\frac{\partial}{\partial \theta_{roll}} \quad \frac{\partial}{\partial \theta_{pitch}} \quad \frac{\partial}{\partial \theta_{yaw}} \right]$ and $[\boldsymbol{\sigma}_\theta]$ the diagonal matrix with the errors of θ_{roll} , θ_{pitch} and θ_{yaw} , i.e., $\sigma_{\theta_{roll}}$, $\sigma_{\theta_{pitch}}$, and $\sigma_{\theta_{yaw}}$.

Evaluating Equation (63), we arrive at the ranging error due to attitude $\sigma_{\dot{\rho}_{ng,\theta}}$ as function of

$$\boldsymbol{\sigma}_\theta = \left[\sigma_{\theta_{roll}} \quad \sigma_{\theta_{pitch}} \quad \sigma_{\theta_{yaw}} \right]^T:$$

$$\sigma_{\dot{\rho}_{ng,\theta}}^{(ECI)} = \sqrt{2} \begin{bmatrix} \Delta \mathbf{a}_{ng,y}^{(SRF)} e_{LOS,z}^{(ECI)} - \Delta \mathbf{a}_{ng,z}^{(SRF)} e_{LOS,y}^{(ECI)} \\ \Delta \mathbf{a}_{ng,x}^{(SRF)} e_{LOS,z}^{(ECI)} - \Delta \mathbf{a}_{ng,z}^{(SRF)} e_{LOS,x}^{(ECI)} \\ \Delta \mathbf{a}_{ng,x}^{(SRF)} e_{LOS,y}^{(ECI)} - \Delta \mathbf{a}_{ng,y}^{(SRF)} e_{LOS,x}^{(ECI)} \end{bmatrix}^T \boldsymbol{\sigma}_\theta. \quad (64)$$

We make the conservative assumption that the amplitude of $\Delta \mathbf{a}_{ng}^{(SRF)}$ is given by the RMS of the non-gravitation accelerations at orbital altitude and take the component with the largest magnitude in each entry of the row vector in Equation (64). We further assume that the amplitude of $e_{LOS}^{(ECI)}$ is 1 and drop the superscript of the reference frame because the errors have the same amplitude in any frame. Equation (64) simplifies to

$$\rho_{\dot{\rho}_{ng,\theta}} = \sqrt{2} \begin{bmatrix} \max \left(\text{RMS}(a_{ng,z}), \text{RMS}(a_{ng,z}) \right) \\ \max \left(\text{RMS}(a_{ng,x}), \text{RMS}(a_{ng,z}) \right) \\ \max \left(\text{RMS}(a_{ng,x}), \text{RMS}(a_{ng,y}) \right) \end{bmatrix}^T \boldsymbol{\sigma}_\theta. \quad (65)$$

In the case of homogenous attitude error, $\sigma_{\theta_{yaw}} = \sigma_{\theta_{pitch}} = \sigma_{\theta_{roll}} \equiv \sigma_\theta$, for example, if there are multiple star tracker cameras and their data is combined optimally with additional attitude sensors, such as an IMU and DWS:

$$\sigma_{\dot{\rho}_{ng,\theta}} = \sqrt{2} \text{RMS}(a_{ng,x}) \sigma_\theta. \quad (66)$$

The values for $\text{RMS}(a_{ng,x})$, $\text{RMS}(a_{ng,y})$ and $\text{RMS}(a_{ng,z})$ we considered in this study are presented in Appendix 8.3 and are functions of the DFC system. We quantify the effect of these errors in Section 5.2 for both electrostatic and quantum accelerometry.

4.2 Gradiometry

In the case of gravity gradiometry, the gravity gradients observed in the satellite reference frame $\mathbf{V}^{(SRF)}$ are related to the gravity gradients in the ECEF reference frame $\mathbf{V}^{(ECEF)}$ by:

$$\mathbf{V}^{(\text{ECEF})} = \mathbf{R}^{(\text{ECEF} \leftarrow \text{SRF})} \mathbf{V}^{(\text{SRF})} \mathbf{R}^{(\text{ECEF} \leftarrow \text{SRF})^T}, \quad (67)$$

where $\mathbf{R}^{(\text{ECEF} \leftarrow \text{SRF})}$ is the rotation that transforms from the satellite to the ECEF reference frame. The attitude measurements generally relate the ICE frame to the SRF frame, so it makes more sense to split the rotation in these frames:

$$\mathbf{V}^{(\text{ECEF})} = \mathbf{R}^{(\text{ECEF} \leftarrow \text{ECI})} \mathbf{R}^{(\text{ECI} \leftarrow \text{SRF})} \mathbf{V}^{(\text{SRF})} \mathbf{R}^{(\text{ECI} \leftarrow \text{SRF})^T} \mathbf{R}^{(\text{ECEF} \leftarrow \text{ECI})^T}. \quad (68)$$

Assuming the ECI to ECEF frame is known perfectly, we can focus on the gravity gradients in the ECI frame:

$$\mathbf{V}^{(\text{ECI})} = \mathbf{R}^{(\text{ECI} \leftarrow \text{SRF})} \mathbf{V}^{(\text{SRF})} \mathbf{R}^{(\text{ECI} \leftarrow \text{SRF})^T}. \quad (69)$$

As for ll-SST, Section 4.1, we model the transformation $\mathbf{R}^{(\text{ECI} \leftarrow \text{SRF})}$ as the product of the error-free rotation $\mathbf{R}^{(\text{ECI} \leftarrow \text{SRF}, \text{true})}$ and a small-angle rotation matrix $\mathbf{\Theta}^{(\text{ECEF} \leftarrow \text{SRF})}$:

$$\mathbf{R}^{(\text{ECI} \leftarrow \text{SRF})} = \mathbf{R}^{(\text{ECI} \leftarrow \text{SRF}, \text{true})} \mathbf{\Theta}^{(\text{ECI} \leftarrow \text{SRF})}, \quad (70)$$

and Equation (67) becomes:

$$\mathbf{V}^{(\text{ECI})} = \mathbf{R}^{(\text{ECI} \leftarrow \text{SRF}, \text{true})} \mathbf{\Theta}^{(\text{ECI} \leftarrow \text{SRF})} \mathbf{V}^{(\text{SRF})} \mathbf{\Theta}^{(\text{ECI} \leftarrow \text{SRF})^T} \mathbf{R}^{(\text{ECI} \leftarrow \text{SRF}, \text{true})^T}. \quad (71)$$

If we restrict our analysis to the terms that contain errors, we can safely ignore the error-free transformation $\mathbf{R}^{(\text{ECI} \leftarrow \text{SRF}, \text{true})}$:

$$\mathbf{V}^{(\text{SRF}, \text{noisy})} = \mathbf{\Theta}^{(\text{ECI} \leftarrow \text{SRF})} \mathbf{V}^{(\text{SRF})} \mathbf{\Theta}^{(\text{ECI} \leftarrow \text{SRF})^T}, \quad (72)$$

We split $\mathbf{\Theta}^{(\text{ECI} \leftarrow \text{SRF})} = \mathbf{E} + \mathbf{I}$ as before and drop the reference frame superscript:

$$\mathbf{V}^{(\text{noisy})} = (\mathbf{I} + \mathbf{E}) \mathbf{V} (\mathbf{I} + \mathbf{E})^T \quad (73)$$

As usual, the error propagation of Equation (73) requires the tensor $\mathbf{V}^{(\text{noisy})}$ to be collapsed into the vector $\mathbf{v}^{(\text{noisy})}$, producing the error 9×9 covariance matrix \mathbf{C}_V :

$$\mathbf{C}_V = \mathbf{\nabla} \mathbf{v}^{(\text{noisy})} [\sigma_\theta] \mathbf{\nabla} \mathbf{v}^{(\text{noisy})^T} \quad (74)$$

In evaluating Equation (74), we assume that \mathbf{V} is error-free, the small angles are negligible $\theta_{\text{roll},s} = \theta_{\text{pitch},s} = \theta_{\text{yaw},s} \approx 0$, and ignore the cross-correlations such that $[\sigma_{V,\theta}] = \text{diag}(\mathbf{C}_V)$, resulting in

$$\begin{bmatrix} \sigma_{V_{xx},\theta}^2 \\ \sigma_{V_{yy},\theta}^2 \\ \sigma_{V_{zz},\theta}^2 \\ \sigma_{V_{xy},\theta}^2 \\ \sigma_{V_{xz},\theta}^2 \\ \sigma_{V_{yz},\theta}^2 \end{bmatrix} = \begin{bmatrix} 0 & 4V_{xz}^2 & 4V_{xy}^2 \\ 4V_{yz}^2 & 0 & 4V_{xy}^2 \\ 4V_{yz}^2 & 4V_{xz}^2 & 0 \\ V_{xz}^2 & V_{yz}^2 & (V_{xx} - V_{yy})^2 \\ V_{xy}^2 & (V_{xx} - V_{zz})^2 & V_{yz}^2 \\ (V_{yy} - V_{zz})^2 & V_{xy}^2 & V_{xz}^2 \end{bmatrix} \begin{bmatrix} \sigma_{\theta_{\text{roll}}}^2 \\ \sigma_{\theta_{\text{pitch}}}^2 \\ \sigma_{\theta_{\text{yaw}}}^2 \end{bmatrix}. \quad (75)$$

Considering the amplitude of the gravity gradient signal presented in Section 8.4 and setting the errors σ_θ equal to 1, the scaling of the attitude errors into gravity gradient errors is

$$[\sigma_{V,\theta}] = \begin{bmatrix} 0.2 & 5 & 3600 \\ & 9.7 & 3603 \\ & & 9.7 \end{bmatrix} \times 10^3 E$$

5 Results and discussion

We present our results by quantifying the amplitude of frame accelerations, i.e., those related to the effect of the Coriolis accelerations and the centrifugal accelerations in Section 5.1. We quantify the errors for ll-SST in Section 5.2 for both electrostatic (Section 5.2.1) and quantum (Section 5.2.2) accelerometers. Finally, we quantify the errors for quantum gradiometry in

Section 5.3 for the gradiometer operating in sequential mode (Section **Error! Reference source not found.**).

5.1 Importance of the frame accelerations

In this section, we quantify the amplitude of the Coriolis and centrifugal accelerations. CAI accelerometry is only affected by the former (Section 3.1.2.1), while gradiometry is affected by both (Section 3.2.2.1).

Recall that the variance of the Coriolis term $\sigma_{\text{Cor},i}^2$ in a CAI accelerometer aligned with the i -axis, cf. Equations (34) and (35), is :

$$\sigma_{\text{Cor},i}^2 = 4\omega_j^2 \sigma_{v_{\text{cloud},k}}^2 + 4\omega_k^2 \sigma_{v_{\text{cloud},j}}^2 + 4\sigma_{\omega,j}^2 v_{\text{cloud},k}^2 + 4\sigma_{\omega,k}^2 v_{\text{cloud},j}^2 \quad (76)$$

which is valid for both along-track and cross-track ll-SST.

In Section 3.1.2.2.2, we discussed the variances $\sigma_{\omega,j}^2$ and $\sigma_{\omega,k}^2$ reflect the angular velocity measurement noise, for which we assume $\sigma_{\omega,j} = \sigma_{\omega,k} = 5 \times 10^{-8}$ rad/s in the case of using the high-performance Astrix 200 laser gyroscope, here assumed to be white noise for simplicity. For the magnitude of the angular velocity after tilting mirror compensation $\delta\omega$, we proposed one order of magnitude worse performance than the errors, i.e., $\delta\omega = 5 \times 10^{-7}$ rad/s, in the *full attitude compensation* scenario. In the *no tilting mirror* scenario, we assume $\omega = 1 \times 10^{-4}$ rad/s for yaw and roll and $\omega = 1.1 \times 10^{-3}$ rad/s for pitch (cf. Section 3.1.2.2.2). We also consider the intermediate case of *minimum pitch-rate compensation*, where pitch is compensated to the level of $\delta\omega = 1 \times 10^{-4}$ rad/s.

For the atom cloud velocity, we assume that either one component is $v_{\text{cloud},j} = 2.5$ cm/s and the other components zero in the case of the concurrent operational mode, or all atom cloud velocity components are zero in the case of the sequential mode of operation (cf. Section 2.3.2.1). For the uncertainty of the atom cloud velocity $\sigma_{v_{\text{cloud}}}$, we assume DKC with $v_{\text{atom,therm}} = 10^{-6}$ m/s and $\sigma_{v_{\text{cloud,initial}}} = 10^{-7}$ m/s (cf. Section 3.1.2.2.1, Equations (38) and (39)), resulting in $\sigma_{v_{\text{cloud,therm}}} = 2.3 \times 10^{-9}$ m/s for $N = 10^4$.

Under these assumptions, we can quantify the effect of the Coriolis term for the concurrent and sequential operational modes combined with different levels of attitude compensation, as summarised in Table 1.

Table 1: Standard deviation of the Coriolis term $\sigma_{\text{Cor},i}$, assuming $\sigma_{\omega,j} = \sigma_{\omega,k} = 5 \times 10^{-8}$ rad/s, $v_{\text{atom,therm}} = 10^{-6}$ m/s and $\sigma_{v_{\text{cloud,initial}}} = 10^{-7}$ m/s for several combinations of angular velocity compensation scenarios and operational modes (affecting the cloud velocity), for the case of along-track ll-SST and the i -axis aligned with the along-track direction.			
Attitude compensation scenario	Residual angular velocity [rad/s]	Concurrent mode	Sequential mode
		[m/s ²] $v_{\text{cloud},k} = \sigma_{v_{\text{cloud,therm}}} = 2.3\text{nm/s}$ $v_{\text{cloud},j} = 2.5\text{cm/s}$	[m/s ²] $v_{\text{cloud},k} = v_{\text{cloud},j} = \sigma_{v_{\text{cloud,therm}}} = 2.3\text{nm/s}$
No tilting mirror	$\omega_j = 1.1 \times 10^{-3}$ $\omega_k = 10^{-4}$	2.5×10^{-9}	2.2×10^{-10}
Minimum pitch-rate compensation	$\delta\omega_j = \omega_k = 10^{-4}$	2.5×10^{-9}	2.8×10^{-11}
Full attitude compensation	$\delta\omega_j = \delta\omega_k = 5 \times 10^{-7}$	2.5×10^{-9}	2.0×10^{-13}

In the concurrent case, the Coriolis effect is dominated by the large cloud velocity and is insensitive to attitude compensation. This means that the only possibility for a CAI

accelerometer to outperform the MicroSTAR accelerometer, which has a precision of $2 \times 10^{-12} \text{ m/s}^2$ (cf. Section 2.3.1.2), is to consider full attitude compensation and zero atom cloud velocity provided by the sequential mode of operation. This choice limits the measurement cycle to be equal to the interrogation time, as explained in Section 2.3.2.1. To make the concurrent mode of operation competitive, one would have to reduce the initial cloud velocity to at least 10^{-5} m/s for the Coriolis effects to reduce to the level of 10^{-12} m/s^2 . This extremely slow velocity would increase the sampling time prohibitively; one may as well cycle through interferometry and atom production in a sequential way. The only other option is to decrease the attitude uncertainty by 3 orders of magnitude, which is very technically challenging for classic attitude sensors.

For CAI gradiometry, the effect of the Coriolis accelerations in Equation (53) is:

$$\sigma_{V_{\text{Cor}}} = \frac{2}{L_{GG}} \sigma_{\text{Cor}}, \quad (77)$$

which effectively means that noise in the gravity gradients is a factor of 4 worse compared to CAI accelerometers, assuming $L_{GG} = 0.5 \text{ m}$. In addition to that, the problem is exacerbated by the small gravity gradient time-variable signal shown in Figure 8. A gradiometer operating in sequential mode with full attitude compensation would have $\sigma_{V_{\text{Cor}}} = 0.8 \text{ mE} = 8.0 \times 10^{-13} \text{ s}^{-2}$, which is insufficient to sense the time-variable gravity field. We note that this discussion is exclusively based on the effect of the Coriolis force, with no regard to the CAI interferometric sensitivity discussed in Section 2.3.2.

The amplitude of the effect of the centrifugal accelerations is $\sigma_{\Omega^2} = \sqrt{8} \delta \omega \sigma_{\omega}$, which follows from Equation (53). Continuing with the assumption that the angular rate has a noise of $\sigma_{\omega} = 5 \times 10^{-8} \text{ rad/s}$ and that ω is related to the tilting mirror compensation $\delta \omega = 5 \times 10^{-7} \text{ rad/s}$, we expect $\sigma_{\Omega^2} = 0.071 \text{ mE}$. Consequently, unlike the Coriolis forces, the centrifugal accelerations do not limit the CAI gradiometer's sensitivity to temporal variations of the gravity field.

5.2 II-SST

In this analysis, we include the effects of attitude uncertainty presented in Section 4.1, for which the magnitude of non-gravitational accelerations is important. We consider the 3 scenarios motivated in Section 8.3: the RMS of the non-gravitational accelerations experienced at 230 km, those experienced roughly at the same altitude with a 1D DFC system similar to GOCE, and the residual non-gravitational accelerations with a 3D DFC system.

5.2.1 Electrostatic accelerometry

We start our analysis of II-SST future gravimetric missions with the case of electrostatic accelerometry. The three DFC scenarios differently amplify the attitude errors σ_{ω} , for which we assume 3 scenarios: DWS of LISA (Section 2.1.3.1), DWS of GRACE-FO (Section 2.1.3.2), and no DWS. In all scenarios, the measurements of the sensors above are optimally combined with the attitude measurements from the star tracker (Section 2.1.1), Astrix 200 laser gyroscope (Section 2.1.2), and accelerometer (Section 2.1.4). The results are shown in Figure 16, along with the errors of the MicroSTAR accelerometer (Section 2.3.1.2) and the predicted performance of the ISR instrument in 2040 (Section 2.2.4).

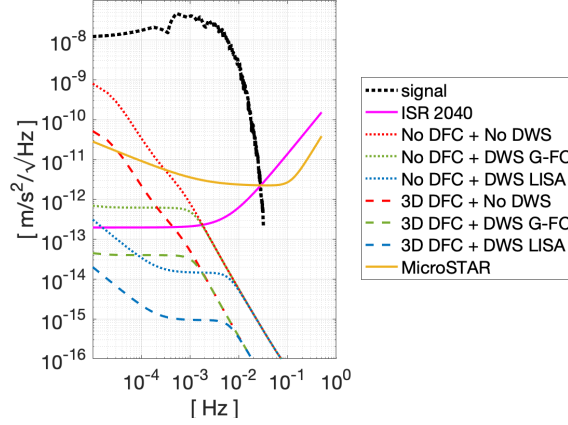


Figure 16: Effect of the attitude errors for no (red, blue and green dotted lines) and 3D (red, blue and green dashed lines) drag-free control (DFC) with three different combinations of attitude instruments indicated in the legend plus the attitude derived from the μ ASC star tracker (Section 2.1.1) and accelerometer (Section 2.1.4), compared to the errors of the accelerometer (Section 2.3.1.2, solid yellow line), ISR errors predicted for 2040 (Section 2.2.4, solid pink line) and the estimated time-variable signal magnitude (dotted black line).

We note that the case of the 1D DFC system has been omitted in Figure 16 because they are identical to the *no DFC* scenario since the y and z-axis non-gravitational accelerations are relevant to the case the ISR axis is (roughly) aligned with the x-direction. Those are the same for both DFC scenarios, cf. Equation (65).

The main message of Figure 16 is that the signal composed of the Atmosphere, Ocean, Hydrology, Ice and Solid-Earth (AOHIS) components of the time-variable gravity field model proposed by Dobslaw et al. (2016), is fully observed until 30mHz, or roughly spherical harmonic (SH) degree 170, assuming sufficiently high dense ground track coverage in a sufficiently short period. At this frequency, the signal represented by the black dotted line crosses both the errors of the ISR instrument and of the accelerometer. More importantly, the high accuracy of the ISR instrument is not utilized below this frequency because of the insufficient accelerometer performance.

The attitude errors are insignificant for the majority of the scenarios. We predict that the need for DFC is only necessary if DWS is not available, which is unlikely since that has already been demonstrated for GRACE-FO. More important are the attitude determination errors, particularly at low frequencies. In this respect, the availability of a DWS is of special importance because it actively reduces the amplitude of attitude errors at low frequencies.

5.2.2 Quantum accelerometry

In order to make complete use of the high accuracy of the ISR instrument predicted for 2040 (Section 2.2.4), we propose the CAI accelerometer indicated in Table 2, with one order of magnitude increase in the number of atoms and the doubling of the momentum space separation. We indicate the updated parameters in bold.

Table 2: CAI parameters: II-SST case.

Parameter	Equation	Symbol	Value
Laser wavelength	(16)	λ	780 nm
Number of atoms	(17)	N	10^7
Interferometer contrast	(17)	C	0.8
Degree of entanglement	(17)	α	0.25
Momentum space separation	(18)	β	2
Interrogation time	(19)	T	5 s

Measurement cycle period	(20)	T_{cycle}	1 s
Atom thermal velocity	(37)(38)	$v_{\text{atom, therm}}$	10^{-6} m/s
Initial cloud velocity error	N/A	$\sigma_{v_{\text{cloud,initial}}}$	10^{-7} m/s
Cloud velocity	(39) Error! Reference source not found.	v_{cloud}	0 or 2.5 cm/s
Attitude accuracy degradation factor	(40)	f_{ω}	10

We selected the parameters in Table 2 so that the noise amplitude of the CAI accelerometer is below the noise floor of the ISR 2040 instrument, as shown in Figure 17. For this analysis, we maintained the DFC and attitude scenarios of Section 5.2.1, with the exception that the accelerometer-derived attitude is not available. For the Coriolis effects, we considered only one scenario: DWS of GRACE-FO (Section 2.1.3.2), tracker (Section 2.1.1), and Astrix 200 laser gyroscope (Section 2.1.2); the case with LISA DWS yields a reduced amplitude of the Coriolis effects (not shown) but with no change to the interpretation of the results.

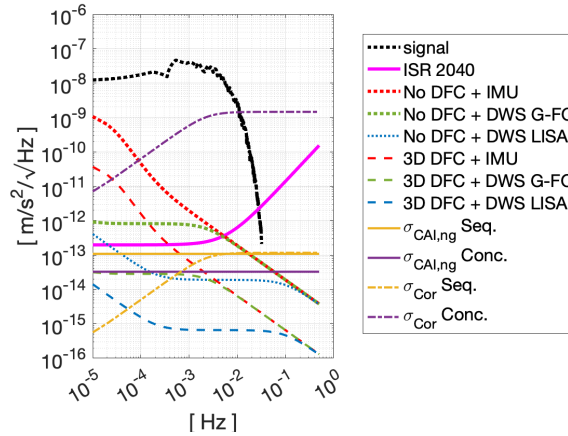


Figure 17: Comparison of the effect of attitude errors (dotted and dashed red, blue and green lines, Section 4.1) with the ISR errors predicted for 2040 (Section 2.2.4, solid pink line, identical to Figure 16) and the estimated time-variable signal magnitude (dotted black line, identical to Figure 16), with the errors of the CAI accelerometer operating under the sequential mode (yellow lines) and concurrent mode (purple lines, cf. Section 2.3.2.1), distinguished between the CAI sensitivity (solid purple and yellow lines, Section 2.3.2) and Coriolis effects (dot-dashed purple and yellow lines, Section 3.1.2)

In the case of the CAI accelerometer operating in concurrent mode, the noise amplitude is dominated by the Coriolis (legend “ $\sigma_{\text{cor Conc.}}$ ”) effect due to the non-zero cloud velocity, as explained in Section 5.1, with a noise floor two orders of magnitude above the CAI sensitivity (legend “ $\sigma_{\text{CAI,ng Conc.}}$ ”). With such an instrument, not even GRACE’s KBR would operate at full capacity, cf. Figure 4. It should be noted that with LISA DWS, it would be possible to use GRACE-FO’s LRI with no reduced performance (not shown). In contrast, this instrument operating in sequential mode has a sensitivity (legend “ $\sigma_{\text{CAI,ng Seq.}}$ ”) a factor of 3 worse than in concurrent mode, as a result of the reduced sampling rate, Equation (20), but a much-reduced effect of the Coriolis accelerations (legend “ $\sigma_{\text{cor Seq.}}$ ”), with a noise floor two orders of magnitude below (4 orders of magnitude if compared to the Coriolis effects of the concurrent mode of operation) and reaching the amplitude of the CAI sensitivity at 3 mHz. As for attitude and DFC options, the situation is much more demanding than electrostatic accelerometry. For quantum accelerometry, there is a need for LISA-level DWS if DFC is unavailable (legend *No DFC + DWS LISA*). If 3D DFC is available, GRACE-FO’s DWS is

sufficient (legend *3D DFC + DWS G-FO*). This illustrates the strict attitude requirements that the increased sensitivity of quantum accelerometers demands.

The temporal signal is resolved up to 30 mHz, or SH degree 170, as is the case with the electrostatic case (Section 5.2.1) because at those frequencies the LRI is the limiting factor. Unlike the electrostatic case, the quantum accelerometer is more accurate than the LRI at all frequencies, and the time-variable signal is measured with a Signal-to-Noise ratio (SNR) of at least 10^4 up to 10 mHz (SH degree 57).

5.3 Gradiometry

Classic gradiometry is not considered because electrostatic accelerometers lack the necessary accuracy to observe the time-variable gravity signal. We consider the same DFC scenario as in Section 5.2.

In Section 5.1, we quantify the effect of the Coriolis accelerations $\sigma_{V_{Cor}}$ under the assumption of white noise for the attitude measured by the Astrix 200 laser gyroscope. In reality, the spectra of the errors of this instrument are far from showing constant amplitude with frequency, cf. Section 2.1.2. Additionally, the combination with other attitude instruments was not quantified. For these reasons, we compare the error spectra of the Coriolis and centrifugal terms with the CAI sensitivity in Table 2, thus making the II-SST and gradiometry case directly comparable. We consider that attitude is measured with the star tracker (Section 2.1.1), Astrix 200 laser gyroscope (Section 2.1.2), and accelerometer (Section 2.1.4). We include the attitude derived from the accelerometer since the demonstration of an early CAI gradiometer in space would benefit from the validation with proven instruments, such as an electrostatic accelerometer.

Additionally, this instrument reduces the amplitude of the attitude errors above 0.7 mHz, cf. Figure 1, which is critical for collecting the small time-variable gravity field disturbances. The results of this analysis are presented in Figure 18.

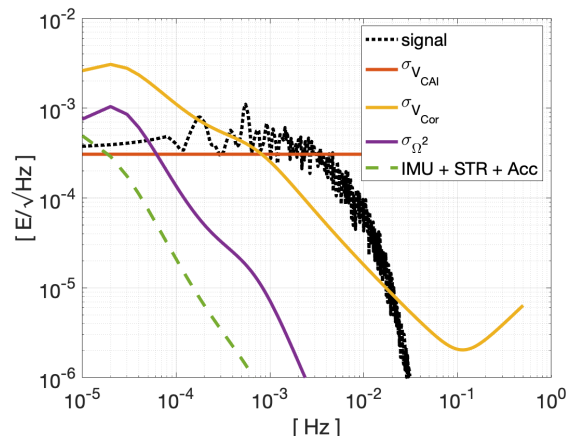


Figure 18: Comparison of the effect of attitude errors (dashed green line, Section 4.2) with the time-variable gravity gradient signal (dotted black line, same as Figure 8) gradiometer CAI sensitivity (red line, Section 3.2.2), the Coriolis effect (yellow line, Section 3.2.2) and the effects of centrifugal accelerations (purple line, Section 3.2.2), as measured by the IMU (Section 2.1.2), star tracker (Section 2.1.1) and attitude derived from the electrostatic accelerometer (Section 2.1.4).

Although the gradiometer CAI sensitivity is barely enough to resolve time-variable gravity signal up to 3 mHz, corresponding roughly to SH degree 17, the Coriolis effects make it impossible to observe this signal below 0.4 mHz or SH degree 2. The effects of attitude uncertainty are at least an order of magnitude below the Coriolis effects and only surpass the magnitude of the gradiometer CAI sensitivity below 0.02 mHz. Of note is that the Coriolis errors (and those associated with centrifugal and attitude errors) are only a function of the attitude sensors and remain the same even if more accurate CAI gradiometers are considered.

In contrast to the II-SST case using quantum accelerometers (Section 5.2.2), where the complete signal spectrum is resolved with a high SNR, the quantum gradiometer with the same CAI parameters is barely able to resolve the time variable signal, with an SNR mostly between 1 and 2, peaking at 3 and dipping at 0.5 at some frequencies.

This example reinforces that the high accuracy of all instruments is critical to the success of CAI gradiometry. Although quantum technology may allow for extremely high CAI sensitivities, a proportional improvement of the attitude sensors is necessary.

6 Summary

In this study, we model the sensitivity of a CAI accelerometer as a function of interferometry contrast, degree of entanglement, number of atoms, momentum space separation and interrogation period (Section 2.3.2). We assume the CAI gradiometer is composed of two CAI accelerometers in the form of two cloud-pairs in the same interferometric chamber. In this way, we model quantum gradiometry in a similar way as classic gradiometry, i.e., that the latter is composed of two electrostatic accelerometers. One important difference is that a CAI accelerometer is inherently a one-dimensional instrument, unlike the electrostatic accelerometer. However, this is irrelevant for the diagonal components of the gravity gradient tensor. With the assumed model for CAI sensitivity, we predict a noise level of $\sigma_{\text{CAI,ng}} = 3.2 \times 10^{-14} \text{m/s}^2$ with the CAI parameters in Table 2, where notably the degree of entanglement is $\alpha = 0.25$, the number of atoms is $N = 10^7$, and the momentum space separation $\beta = 2$ associated with a second atom. This example scenario intends to illustrate a possible path for the development of CAI instruments with increasing accuracy and their capabilities for gradiometry, which are discussed in the following paragraphs.

In order to reduce the effects of inaccurately known attitude rates on Coriolis accelerations in quantum instruments, defined analytically in Section 3.1.2.1 for CAI accelerometers and in Section 3.2.2.1 for CAI gradiometers, we distinguish between concurrent and sequential modes of operation, with the former allowing for a higher sampling rate and accuracy. The latter minimises atom cloud velocity and, consequently, Coriolis accelerations (Section 2.3.2.1). In Section 5.1, we demonstrate that CAI accelerometry operating in the concurrent mode results in prohibitively high effects resulting from the Coriolis accelerations, limiting the sensitivity of any CAI accelerometer to $\sigma_{\text{Cor}} = 2.5 \times 10^{-9} \text{m/s}^2$, for which we assume an initial cloud velocity error of $\sigma_{v_{\text{cloud,initial}}} = 10^{-7} \text{m/s}$, a thermal cloud velocity of $v_{\text{atom,therm}} = 10^{-6} \text{m/s}$ and transverse cloud velocity of $v_{\text{cloud}} = 2.5 \text{cm/s}$. For the sequential mode of operation, the cloud velocity is solely associated with thermal motion, and the Coriolis effects are limited to $\sigma_{\text{Cor}} = 2.0 \times 10^{-13} \text{m/s}^2$, including the effect of a lower sampling rate than the concurrent operational mode. This requires full attitude compensation with tilting mirrors, which reduce the satellite's attitude rates down to $\delta\omega = 5 \times 10^{-7} \text{rad/s}$, assumed to be one order of magnitude worse than what the high-performance Astrix 200 laser gyroscope can measure (Section 2.1.2). Although such a CAI instrument is well suited as an accelerometer for II-SST, it is unable to measure temporal gravity changes as a gradiometer since the sensitivity would be limited to $\sigma_{V_{\text{Cor}}} = 0.8 \text{mE}$ for a distance between cloud-pairs (i.e., the gradiometer arm length) of $L_{GG} = 0.5 \text{m}$. In Section 5.2.2, we consider a CAI accelerometer with increased performance operating in sequential mode to have a sensitivity of $\sigma_{\text{CAI,ng}} = 1.1 \times 10^{-13} \text{m/s}^2$ that is not significantly limited by the effects of the Coriolis accelerations, since they have an amplitude of $\sigma_{\text{Cor}} = 1.2 \times 10^{-13} \text{m/s}^2$. This means that the LRI predicted for 2040 is not hampered in any way, down to the sub-orbital frequencies. In contrast, in the case of II-SST with an electrostatic accelerometer, Section 5.2.1, the MicroSTAR electrostatic accelerometer dominates the noise spectrum in all the frequencies below 30 mHz. Of note is that in either case, the signal amplitude is at least two orders of

magnitude above the total noise, and the system is sensitive to the temporal gravity field up to SH degree 170.

We presented electrostatic and quantum accelerometers for II-SST and gradiometer satellite mission concepts, modelling the measurements and their errors analytically (Section 3). The attitude determination was given special attention, particularly the modelling of the accelerometers and gradiometers for this purpose, as well as associated errors. For electrostatic accelerometers, the instrument provides attitude information directly since there are multiple electrodes in each facet of the proof mass cavity (Section 2.1.4). On the other hand, no attitude data can be measured by a quantum accelerometer. For classic gradiometry, attitude is estimated with one order of magnitude better accuracy than the electrostatic accelerometer (Section 3.2.1.2). For quantum gradiometry, we demonstrate that 12 uniaxial CAI gradiometers are needed to uniquely resolve the attitude of the satellite (Section 3.2.2.2).

We considered the errors related to the rotation of the measurements in the body (for gradiometry) or local (for II-SST) frames to the Earth corotating frame (Section 4), which are of importance given the high accuracy of the measurements and the potential large acceleration or gravity gradient signal at LEO altitudes. These errors tie the signal amplitude of non-gravitational accelerations (for the case of accelerometers) or gravity gradient amplitudes (for gradiometry) with the attitude accuracy. For those cases when attitude measurements have limited accuracy, e.g., classic attitude sensors, while the signal can be measured with increased accuracy, e.g., quantum sensors, these errors become important. This is the case with II-SST equipped with a CAI accelerometer, Section 5.2.2, where the need for a 3D DFC system is required in the case the attitude derived with the DWS is retrieved with accuracy comparable to what GRACE-FO is capable; if this can be done with an accuracy predict for LISA, then no DFC is necessary. For quantum gradiometers, the attitude errors are not significant, as shown in Section 5.3. We apply the CAI parameters derived for the case of II-SST to quantum gradiometry in Section **Error! Reference source not found.**, using the CAI operating in sequential mode. We demonstrated that, unlike the case for II-SST, this instrument is barely sensitive enough to resolve temporal changes in Earth's gravity. The maximum SH degree it is sensitive to is 17, and the Coriolis accelerations make it impossible to measure spatial features with length associated with SH degree 2 or longer. This is an illustrative example of the much-reduced gravity gradient signal amplitude, compared to gravitational accelerations, to which II-SST is sensitive.

We recognise that there are important technological challenges associated with the solutions considered in this study. We have generally neglected such details because we restrict our analysis to the conceptual level. The obvious consequence is the high cost for the necessary technical and engineering developments, most notably those associated with i) the highly accurate rotation compensation provided by the tilting mirrors and ii) the colling of the atom cloud during the BEC preparation that is required to reduce the thermal velocity of the atoms as assumed in this study. We also note that we did not model the loss of interferometric contrast associated with the scenarios without rotation compensation since that parameter is specific to the design of the instrument.

Nevertheless, we have demonstrated that the effects of inaccurately measured attitude in the Coriolis accelerations are of paramount importance to the success of the CAI satellite gravimetry, such that any CAI concept operating in concurrent mode can never have its sensitivity accurately determined, even in the quiet environment of space. For demonstration purposes of CAI technology to measure the time-variable gravity field, the best option is the II-SST measurement concepts and a CAI accelerometer operating in sequential mode because

this requires less demanding CAI parameters. With the progress of laser metrology, this is still the best option to ensure the accuracy of the LRI instrument is fully exploited since the parallel development of CAI technology allows for comparable accuracies.

7 Acknowledgements

The work presented in this paper was conducted in the frames of the European Space Agency (ESA) study entitled *Quantum Space Gravimetry for monitoring Earth's Mass Transport Processes* (QSG4EMT). The QSG4EMT study has the objective to analyse QSG mission architectures that can optimally recover the time variable gravity field of the Earth, which relates to mass transport processes of interest for operational applications, as well as for Earth Sciences, and propose candidate QSG mission concepts with mission requirements that advance the science and satisfy the needs of the user community to a greater extent than the state-of-the-art and planned missions.

We thank Vitali Müller, from Albert-Einstein-Institut in Hannover, for the insightful predictions of the LRI performance in the near future.

8 Appendix

8.1 Derivations

8.1.1 CAI accelerometer observation equation

Assume that the axis of the Raman laser is aligned with the i -axis:

$$\frac{\mathbf{k}_{\text{eff}}}{k_{\text{eff}}} = \mathbf{e}_i.$$

Starting from Equation (25):

$$\Phi = \mathbf{k}_{\text{eff}} \cdot (\mathbf{a}_{\text{cloud}} - \mathbf{a}_{\text{mirror}}) T^2$$

The non-gravitation accelerations $\mathbf{a}_{\text{ng}} = \mathbf{a}_{\text{mirror}}$ project along \mathbf{e}_i are given by:

$$\Phi = \mathbf{k}_{\text{eff}} \cdot (\mathbf{a}_{\text{cloud}} - \mathbf{a}_{\text{ng}}) T^2$$

$$\frac{\Phi}{k_{\text{eff}}} = \frac{\mathbf{k}_{\text{eff}}}{k_{\text{eff}}} \cdot (\mathbf{a}_{\text{cloud}} - \mathbf{a}_{\text{ng}}) T^2$$

$$\frac{\Phi}{k_{\text{eff}} T^2} = \mathbf{e}_i \cdot (\mathbf{a}_{\text{cloud}} - \mathbf{a}_{\text{ng}}) = \mathbf{e}_i \cdot \mathbf{a}_{\text{cloud}} - \mathbf{e}_i \cdot \mathbf{a}_{\text{ng}}$$

$$\mathbf{e}_i \cdot \mathbf{a}_{\text{ng}} = -\frac{\Phi}{k_{\text{eff}} T^2} + \mathbf{e}_i \cdot \mathbf{a}_{\text{cloud}}$$

Replacing the acceleration of the atom cloud is given by Equation (27) in the equation above, which results in Equation (31):

$$\mathbf{e}_i \cdot \mathbf{a}_{\text{ng}} = -\frac{\Phi}{k_{\text{eff}} T^2} + \mathbf{e}_i \cdot \left(-(V - \Omega^2 - \dot{\Omega})(\mathbf{r}_{\text{cloud}} - \mathbf{r}_{\text{CoM}}) + 2\boldsymbol{\omega} \times \mathbf{v}_{\text{cloud}} \right)$$

8.1.2 CAI gradiometer observation equation

From Equation (48):

$$\frac{\Phi_{i,l}}{k_{\text{eff}} T^2} = \mathbf{e}_i \cdot \left(-\mathbf{a}_{\text{ng},l} - (V - \Omega^2 - \dot{\Omega})(\mathbf{r}_{\text{cloud},l} - \mathbf{r}_{\text{CoM}}) + 2\boldsymbol{\omega} \times \mathbf{v}_{\text{cloud},l} \right),$$

the phase measurement of cloud l is:

$$\Phi_{i,l} = k_{\text{eff}} T^2 \mathbf{e}_i \cdot \left(-\mathbf{a}_{\text{ng},l} - (V - \Omega^2 - \dot{\Omega})(\mathbf{r}_{\text{cloud},l} - \mathbf{r}_{\text{CoM}}) + 2\boldsymbol{\omega} \times \mathbf{v}_{\text{cloud},l} \right),$$

and the differential measurement $\delta\Phi_i$ is:

$$\begin{aligned} \delta\Phi_i &\equiv \Phi_{i,1} - \Phi_{i,2} = \\ &k_{\text{eff}} T^2 \mathbf{e}_i \cdot \left(-\mathbf{a}_{\text{ng},1} - (V - \Omega^2 - \dot{\Omega})(\mathbf{r}_{\text{cloud},1} - \mathbf{r}_{\text{CoM}}) + 2\boldsymbol{\omega} \times \mathbf{v}_{\text{cloud},1} \right) - \\ &k_{\text{eff}} T^2 \mathbf{e}_i \cdot \left(-\mathbf{a}_{\text{ng},2} - (V - \Omega^2 - \dot{\Omega})(\mathbf{r}_{\text{cloud},2} - \mathbf{r}_{\text{CoM}}) + 2\boldsymbol{\omega} \times \mathbf{v}_{\text{cloud},2} \right) \end{aligned}$$

If \mathbf{r} is measured from the CoM, $\mathbf{v}_{\text{cloud},1}$ and $\mathbf{v}_{\text{cloud},2}$ are both given by $\mathbf{v}_{\text{cloud,therm}}$ (assumed to be a random variable):

$$\frac{\delta\Phi_i}{k_{\text{eff}}T^2} = \mathbf{e}_i \cdot \left(-\mathbf{a}_{\text{ng},1} + \mathbf{a}_{\text{ng},2} - (\mathbf{V} - \boldsymbol{\Omega}^2 - \dot{\boldsymbol{\Omega}})\delta\mathbf{r}_{\text{cloud}} + 2\boldsymbol{\omega} \times \mathbf{v}_{\text{cloud,therm}} \right)$$

Since $\mathbf{a}_{\text{ng},1} = \mathbf{a}_{\text{ng},2}$ and $\delta\mathbf{r}_{\text{cloud}} = L_{\text{GG}}\mathbf{e}_i$, we arrive at Equation (50):

$$\frac{\delta\Phi_i}{k_{\text{eff}}T^2} = \mathbf{e}_i \cdot \left(-(\mathbf{V} - \boldsymbol{\Omega}^2 - \dot{\boldsymbol{\Omega}})L_{\text{GG}}\mathbf{e}_i + 2\boldsymbol{\omega} \times \mathbf{v}_{\text{cloud,therm}} \right)$$

The scalar evaluation of this expression requires:

$$\begin{aligned} \mathbf{V}\mathbf{e}_i &= \begin{bmatrix} V_{ii} \\ V_{ij} \\ V_{ik} \end{bmatrix} \text{ and } \mathbf{e}_i \cdot (\mathbf{V}\mathbf{e}_i) = V_{ii}, \\ \boldsymbol{\Omega}^2\mathbf{e}_i &= \begin{bmatrix} -\omega_j^2 - \omega_k^2 \\ \omega_i\omega_j \\ \omega_i\omega_k \end{bmatrix} \text{ and } \mathbf{e}_i \cdot (\boldsymbol{\Omega}^2\mathbf{e}_i) = -\omega_j^2 - \omega_k^2, \\ \dot{\boldsymbol{\Omega}}\mathbf{e}_i &= \begin{bmatrix} 0 \\ \dot{\omega}_k \\ \dot{\omega}_j \end{bmatrix} \text{ and } \mathbf{e}_i \cdot (\dot{\boldsymbol{\Omega}}\mathbf{e}_i) = 0, \\ \boldsymbol{\omega} \times \mathbf{v} &= \begin{bmatrix} \omega_j v_k - \omega_k v_j \\ \omega_k v_i - \omega_i v_k \\ \omega_i v_j - \omega_j v_i \end{bmatrix} \text{ and } \mathbf{e}_i \cdot (\boldsymbol{\omega} \times \mathbf{v}) = \omega_j v_k - \omega_k v_j, \end{aligned}$$

resulting in:

$$\begin{aligned} \frac{\delta\Phi_i}{k_{\text{eff}}T^2} &= -(V_{ii} + \omega_j^2 + \omega_k^2)L_{\text{GG}} + 2\omega_j v_{\text{cloud,therm},k} - 2\omega_k v_{\text{cloud,therm},j} \\ \frac{\delta\Phi_i}{k_{\text{eff}}T^2} \frac{1}{L_{\text{GG}}} &= -V_{ii} - \omega_j^2 - \omega_k^2 + \frac{2}{L_{\text{GG}}}\omega_j v_{\text{cloud,therm},k} - \frac{2}{L_{\text{GG}}}\omega_k v_{\text{cloud,therm},j} \end{aligned}$$

Rearranging, produces Equation (51):

$$V_{ii} = -\frac{1}{L_{\text{GG}}}\frac{\delta\Phi_i}{k_{\text{eff}}T^2} - \omega_j^2 - \omega_k^2 + \frac{2}{L_{\text{GG}}}(\omega_j v_{\text{cloud,therm},k} - \omega_k v_{\text{cloud,therm},j})$$

For a CAI gradiometer oriented along the other axes:

$$V_{jj} = -\frac{1}{L_{\text{GG}}}\frac{\delta\Phi_j}{k_{\text{eff}}T^2} - \omega_k^2 - \omega_i^2 + \frac{2}{L_{\text{GG}}}(\omega_k v_{\text{cloud,therm},i} - \omega_i v_{\text{cloud,therm},k}),$$

$$V_{kk} = -\frac{1}{L_{\text{GG}}}\frac{\delta\Phi_k}{k_{\text{eff}}T^2} - \omega_i^2 - \omega_j^2 + \frac{2}{L_{\text{GG}}}(\omega_i v_{\text{cloud,therm},j} - \omega_j v_{\text{cloud,therm},i}),$$

derived considering the following relations:

$$\begin{aligned} \mathbf{e}_j \cdot (\mathbf{V}\mathbf{e}_j) &= V_{jj} \text{ and } \mathbf{e}_k \cdot (\mathbf{V}\mathbf{e}_k) = V_{kk} \\ \mathbf{e}_j \cdot (\boldsymbol{\Omega}^2\mathbf{e}_j) &= -\omega_i^2 - \omega_k^2 \text{ and } \mathbf{e}_k \cdot (\boldsymbol{\Omega}^2\mathbf{e}_k) = -\omega_i^2 - \omega_j^2 \\ \mathbf{e}_j \cdot (\dot{\boldsymbol{\Omega}}\mathbf{e}_j) &= \mathbf{e}_k \cdot (\dot{\boldsymbol{\Omega}}\mathbf{e}_k) = 0 \\ \mathbf{e}_j \cdot (\boldsymbol{\omega} \times \mathbf{v}) &= \omega_k v_i - \omega_i v_k \text{ and } \mathbf{e}_k \cdot (\boldsymbol{\omega} \times \mathbf{v}) = \omega_i v_j - \omega_j v_i \end{aligned}$$

8.2 Angular Velocity Signal magnitude

To assess the signal size of the angular velocity, we make several assumptions on the orbit and attitude control. First, we assume an orbit at an altitude of 500 km, which gives an orbital period of $T_{\text{orb}} = 95 \text{ min}$. Next, we assume that the satellite is nadir pointing, which results in a mean pitch rate of:

$$\text{mean}(\omega_y) = 2\pi/T_{\text{orb}} = 1.1 \text{ mrad/s.} \quad (78)$$

Further, we assume that the satellite is pointing in the direction of atmospheric flow to minimise the effects of drag. The direction of the flow relative to the satellite is composed of the inertial velocity of 7.6 km/s and the corotation of the atmosphere of 500 m/s at the equator in an eastward direction. The worst case is a polar orbit, in which the inertial velocity is perpendicular to the velocity of the corotating atmosphere. The maximum yaw angle at the equator is $\arcsin(0.5 \text{ km}/7.6 \text{ km}) = 3.77^\circ$. Since the velocity of the corotating atmosphere is zero at the pole, the yaw angle will also be zero. Thus, the yaw angle changes from 3.77° to 0° during a quarter of an orbit, i.e., by $3.77^\circ/(T_{orb}/4) = 4.6 \times 10^{-5} \text{ rad/s}$. To calculate the RMS of the angular velocity, we assume that the yaw angle varies like a sine function with an orbital period, i.e.:

$$\psi = 3.77^\circ \sin(2\pi t/T_{orb}). \quad (79)$$

The angular velocity is the time derivative of that function:

$$\omega_z = \frac{\partial \psi}{\partial t} = 3.77^\circ 2\pi/T_{orb} \cos(2\pi t/T_{orb}). \quad (80)$$

The integral of the squared function is:

$$\begin{aligned} \int_0^{T_{orb}} \omega_z dt &= (3.77^\circ 2\pi/T_{orb})^2 \int_0^{T_{orb}} \cos^2(2\pi t/T_{orb}) dt \\ &= (3.77^\circ 2\pi/T_{orb})^2 \frac{1}{2} \int_0^{T_{orb}} 1 - \sin(4\pi t/T_{orb}) dt \\ &= (3.77^\circ 2\pi/T_{orb})^2 \frac{1}{2} [t - 4\pi/T_{orb} \cos(4\pi t/T_{orb})]_0^{T_{orb}} \\ &= (3.77^\circ 2\pi/T_{orb})^2 T_{orb}/2. \end{aligned} \quad (81)$$

The RMS is then the square root of the integral divided by T_{orb} :

$$RMS(\omega_z) = \sqrt{\frac{1}{T_{orb}} \int_0^{T_{orb}} \omega_z dt} = 3.77^\circ \frac{2\pi}{T_{orb}\sqrt{2}} = 5.1 \times 10^{-5} \text{ rad/s}. \quad (82)$$

When magnetic torquers are the only means for attitude control, there is typically no control of the roll at the equator because the magnetic field lines are parallel to the roll axis. With that in mind, we assume that the RMS of the roll rate is:

$$RMS(\omega_x) = 0.1 \text{ mrad/s}.$$

8.3 Non-gravitational acceleration signal magnitude

Some of the error propagations require assumptions of the non-gravitational acceleration signal size. Considering that aerodynamic accelerations are large at low altitudes, we use GOCE data as a worst-case scenario. Typical acceleration signal sizes are reported in Table 3.

Table 3: Non-gravitational signal size in nm/s^2 , mean for long-track and standard deviation for cross-track and radial directions, for the case of the GOCE mission, considering 1D and (hypothetical) 3D drag control (Visser and van den IJssel 2016).

[nm/s^2]	GOCE 230km	1D Drag Control	3D Drag Control
Along-track (mean)	10000	10	10
Cross-track (STD)	289	289	10
Radial (STD)	22	22	10

Referring to Christoph Steiger, Mardle, and Emanuelli (2014), the DFC of GOCE was estimated to reduce non-gravitation accelerations down to 1 nm/s^2 . As such, the assumptions on 1D and 3D DFC shown in Table 3 are conservative.

8.4 Gravity gradient signal magnitude

Assuming a LEO orbit, the signal amplitude of the (symmetric) gravity gradient tensor in the LHRF $\mathbf{V}^{(\text{LHRF})}$ at 450km altitude is (e.g. Rosen 2021):

$$\text{RMS}(\mathbf{V}^{(\text{LHRF})}) \approx \begin{bmatrix} 1200 & 0 & 0 \\ & 1200 & 0 \\ & & 2400 \end{bmatrix} + \begin{bmatrix} 3.01 & 0.03 & 0.09 \\ & 4.22 & 4.38 \\ & & 7.23 \end{bmatrix} [E].$$

The first term is associated with the signal caused by the central term of the gravity field, and the static gravity field of the Earth causes the second term. We ignored the term caused by the temporal variations of the gravity field.

Abbreviations and Acronyms

ASD	Amplitude Spectral Density
BEC	Bose-Einstein Condensate
CAI	Cold Atom Interferometer (or interferometry)
CoM	Centre of Mass
DKC	Delta Kick-Collimation
DFC	Drag-Free Control
DWS	Differential wavefront sensor
ECEF	Earth-centred, Earth-fixed (reference frame)
ECI	Earth-centred, inertial (reference frame)
ESA	European Space Agency
GG	Gravity Gradiometry
GOCE	Gravity field and steady-state Ocean Circulation Explorer
GRACE	Gravity and Climate Experiment
GRACE-FO	Gravity and Climate Experiment Follow-On
ECEF	Earth-centred, Earth-fixed
ECI	Earth-centred, inertial
IMU	Inertial Measurement Unit
ICE	Interférométrie atomique à sources Cohérentes pour l'Espace
ISR	Inter-satellite range/ranging
KBR	K-Band Ranging
LEO	Low-Earth Orbit
LOS	Line-Of-Sight
LRI	Laser ranging instrument
ll-SST	low-low Satellite-to-Satellite Tracking
LHRF	Local Horizontal reference frame
MAIUS	Matter-Wave Interferometry in Weightlessness
μ ASC	Micro Advanced Stellar Compass
MOT	Magneto-Optical Trap
NGGM	Next Generation Gravity Mission
QSG	Quantum Space Gravimetry
QSG4EMT	Quantum Space Gravimetry for monitoring Earth Mass Transport processes
QT	Quantum Technology
PSD	Power Spectral Density
RMS	Root Mean Square
SH	Spherical Harmonic
SRF	Satellite Reference Frame
TMA	Triple Mirror Assembly

References

- Abend, Sven, Baptiste Allard, Aidan S. Arnold, Ticijana Ban, Liam Barry, Baptiste Battelier, Ahmad Bawamia, et al. 2023. "Technology Roadmap for Cold-Atoms Based Quantum Inertial Sensor in Space." *AVS Quantum Science* 5 (1). <https://doi.org/10.1116/5.0098119>.
- Abich, Klaus, Alexander Abramovici, Bengie Amparan, Andreas Baatzsch, Brian Bachman Okihiro, David C. Barr, Maxime P. Bize, et al. 2019. "In-Orbit Performance of the GRACE Follow-on Laser Ranging Interferometer." *Physical Review Letters* 123 (3): 031101. <https://doi.org/10.1103/PhysRevLett.123.031101>.
- Airbus. 2022. "ASTRIX® 200 Specification Sheet." https://www.airbus.com/sites/g/files/jlcbita136/files/2022-02/ScE-AVIONICS-ASTRIX200v3_2022.pdf.
- Amri, Sirine. 2022. "Optimized Matter-Wave Lensing of Quantum Gases for Precision Atom Sensors." Doctorate dissertation, Université Paris-Saclay. <https://theses.hal.science/tel-03852963>.
- Carraz, Olivier, Christian Siemes, Luca Massotti, Roger Haagmans, and Pierluigi Silvestrin. 2014. "A Spaceborne Gravity Gradiometer Concept Based on Cold Atom Interferometers for Measuring Earth's Gravity Field." *Atomic Physics. Microgravity Science and Technology* 26 (3): 139–45. <https://doi.org/10.1007/s12217-014-9385-x>.
- Cesare, Stefano, Sabrina Dionisio, Massimiliano Saponara, David Bravo-Berguño, Luca Massotti, João Teixeira da Encarnação, and Bruno Christophe. 2022. "Drag and Attitude Control for the Next Generation Gravity Mission." *Remote Sensing* 14 (12): 2916. <https://doi.org/10.3390/rs14122916>.
- Christoph Steiger, Nic Mardle, and Pier Paolo Emanuelli. 2014. "GOCE End-of-Mission Operations Report." GO-RP-ESC-FS-6268.
- Christophe, B., B. Foulon, F. Liorzou, V. Lebat, D. Boulanger, P.-A. Huynh, N. Zahzam, Y. Bidet, and A. Bresson. 2018. "Status of Development of the Future Accelerometers for Next Generation Gravity Missions." In *International Association of Geodesy Symposia*, 149:85–89. https://doi.org/10.1007/1345_2018_42.
- Dahl, Katrin, Pelin Cebeci, Oliver Fitzau, Martin Giesberts, Christian Greve, Markus Krutzik, Achim Peters, et al. 2019. "A New Laser Technology for LISA." In *International Conference on Space Optics — ICSO 2018*, edited by Nikos Karafolas, Zoran Sodnik, and Bruno Cugny, 11180:11. SPIE. <https://doi.org/10.1117/12.2535931>.
- Dobslaw, Henryk, Inga Bergmann-Wolf, Ehsan Forootan, Christoph Dahle, Torsten Mayer-Gürr, Jürgen Kusche, and Frank Flechtner. 2016. "Modeling of Present-Day Atmosphere and Ocean Non-Tidal de-Aliasing Errors for Future Gravity Mission Simulations." *Journal of Geodesy* 90 (5): 423–36. <https://doi.org/10.1007/s00190-015-0884-3>.
- Douch, Karim, Hu Wu, Christian Schubert, Jürgen Müller, and Franck Pereira dos Santos. 2018. "Simulation-Based Evaluation of a Cold Atom Interferometry Gradiometer Concept for Gravity Field Recovery." *Advances in Space Research* 61 (5): 1307–23. <https://doi.org/10.1016/j.asr.2017.12.005>.
- Goswami, Sujata, Samuel P. Francis, Tamara Bandikova, and Robert E. Spero. 2021. "Analysis of GRACE Follow-On Laser Ranging Interferometer Derived Inter-Satellite Pointing Angles." *IEEE Sensors Journal* 21 (17): 19209–21. <https://doi.org/10.1109/JSEN.2021.3090790>.
- Groh, Andreas, Martin Horwath, Alexander Horwath, Rakia Meister, Louise Sandberg Sørensen, Valentina R. Barletta, René Forsberg, et al. 2019. "Evaluating GRACE Mass Change Time Series for the Antarctic and Greenland Ice Sheet—Methods and Results." *Geosciences* 9 (10): 415. <https://doi.org/10.3390/geosciences9100415>.

- Gross, Christian. 2012. "Spin Squeezing, Entanglement and Quantum Metrology with Bose–Einstein Condensates." *Journal of Physics B: Atomic, Molecular and Optical Physics* 45 (10): 103001. <https://doi.org/10.1088/0953-4075/45/10/103001>.
- Han, S.-C. 2006. "Crustal Dilatation Observed by GRACE After the 2004 Sumatra-Andaman Earthquake." *Science* 313 (5787): 658–62. <https://doi.org/10.1126/science.1128661>.
- Heller-Kaikov, Betty, Roland Pail, and Ilias Daras. 2023. "Mission Design Aspects for the Mass Change and Geoscience International Constellation (MAGIC)." *Geophysical Journal International* 186 (2): 227–36. <https://doi.org/10.1093/gji/ggad266>.
- Herceg, M., P. S. Jørgensen, and J. L. Jørgensen. 2017. "Characterization and Compensation of Thermo-Elastic Instability of SWARM Optical Bench on Micro Advanced Stellar Compass Attitude Observations." *Acta Astronautica* 137 (April): 205–13. <https://doi.org/10.1016/j.actaastro.2017.04.018>.
- Jiang, Dong, Jianhua Wang, Yaohuan Huang, Kang Zhou, Xiangyi Ding, and Jingying Fu. 2014. "The Review of GRACE Data Applications in Terrestrial Hydrology Monitoring." *Advances in Meteorology* 2014: 1–9. <https://doi.org/10.1155/2014/725131>.
- Kaltenbaek, Rainer, Antonio Acin, Laszlo Bacsardi, Paolo Bianco, Philippe Bouyer, Eleni Diamanti, Christoph Marquardt, et al. 2021. "Quantum Technologies in Space." *Experimental Astronomy* 51 (3): 1677–94. <https://doi.org/10.1007/s10686-021-09731-x>.
- Knabe, Annike, Manuel Schilling, Hu Wu, Alireza HosseiniArani, Jürgen Müller, Quentin Beaufils, and Franck Pereira dos Santos. 2022. "The Benefit of Accelerometers Based on Cold Atom Interferometry for Future Satellite Gravity Missions." In *International Association of Geodesy Symposia*, 213–20. https://doi.org/10.1007/1345_2022_151.
- Kornfeld, Richard P., Bradford W. Arnold, Michael A. Gross, Neil T. Dahya, William M. Klipstein, Peter F. Gath, and Srinivas Bettadpur. 2019. "GRACE-FO: The Gravity Recovery and Climate Experiment Follow-On Mission." *Journal of Spacecraft and Rockets* 56 (3): 931–51. <https://doi.org/10.2514/1.A34326>.
- Malossi, N., Q. Bodart, S. Merlet, T. Lévêque, A. Landragin, and F. Pereira Dos Santos. 2010. "Double Diffraction in an Atomic Gravimeter." *Physical Review A* 81 (1): 013617. <https://doi.org/10.1103/PhysRevA.81.013617>.
- Massotti, Luca, Christian Siemes, Günther March, Roger Haagmans, and Pierluigi Silvestrin. 2021. "Next Generation Gravity Mission Elements of the Mass Change and Geoscience International Constellation: From Orbit Selection to Instrument and Mission Design." *Remote Sensing* 13 (19): 3935. <https://doi.org/10.3390/rs13193935>.
- Müntinga, H., H. Ahlers, M. Krutzik, A. Wenzlawski, S. Arnold, D. Becker, K. Bongs, et al. 2013. "Interferometry with Bose-Einstein Condensates in Microgravity." *Physical Review Letters* 110 (9): 093602. <https://doi.org/10.1103/PhysRevLett.110.093602>.
- Nicklaus, K., S. Cesare, L. Massotti, L. Bonino, S. Mottini, M. Pisani, and P. Silvestrin. 2019. "Laser Metrology Concept Consolidation for NGGM." In *International Conference on Space Optics — ICSO 2018*, edited by Nikos Karafolas, Zoran Sodnik, and Bruno Cugny, 11180:151. SPIE. <https://doi.org/10.1117/12.2536071>.
- Peters, Achim, KY Chung, Steven Chu, and San Francisco. 1999. "Measurement of Gravitational Acceleration by Dropping Atoms." *Nature* 400: 849–52. <https://doi.org/10.1038/23655>.
- Rosen, Mitchell David. 2021. "Analysis of Hybrid Satellite-to-Satellite Tracking and Quantum Gravity Gradiometry Architecture for Time-Variable Gravity Sensing Missions." Master Thesis, University of Texas at Austin.
- Rummel, Reiner, Weiyong Yi, and Claudia Stummer. 2011. "GOCE Gravitational Gradiometry." *Journal of Geodesy* 85 (11): 777–90. <https://doi.org/10.1007/s00190-011-0500-0>.
- Schütze, D., G. Stede, V. Müller, O. Gerberding, C. Mahrtdt, B. Sheard, G. Heinzl, and K. Danzmann. 2013. "LISA-like Laser Ranging for GRACE Follow-On." *Astronomical*

- Society of the Pacific Conference Proceedings* 467 (2003): 285–90.
<http://www.apc.univ-paris7.fr/~beckmann/Proceedings/Schutze.pdf>.
- Sheard, B. S., G. Heinzel, K. Danzmann, D. A. Shaddock, W. M. Klipstein, and W. M. Folkner. 2012. “Intersatellite Laser Ranging Instrument for the GRACE Follow-on Mission.” *Journal of Geodesy* 86 (12): 1083–95. <https://doi.org/10.1007/s00190-012-0566-3>.
- Stummer, C., T. Fecher, and R. Pail. 2011. “Alternative Method for Angular Rate Determination within the GOCE Gradiometer Processing.” *Journal of Geodesy* 85 (9): 585–96. <https://doi.org/10.1007/s00190-011-0461-3>.
- Szigeti, Stuart S., Onur Hosten, and Simon A. Haine. 2021. “Improving Cold-Atom Sensors with Quantum Entanglement: Prospects and Challenges.” *Applied Physics Letters* 118 (14): 1–18. <https://doi.org/10.1063/5.0050235>.
- Teixeira da Encarnação, João, Himanshu Save, Byron Tapley, and Hyung-Jin Rim. 2020. “Accelerometer Parameterization and the Quality of Gravity Recovery and Climate Experiment Solutions.” *Journal of Spacecraft and Rockets* 57 (4): 740–52. <https://doi.org/10.2514/1.A34639>.
- Trimeche, A., B. Battelier, D. Becker, A. Bertoldi, P. Bouyer, C. Braxmaier, E. Charron, et al. 2019. “Concept Study and Preliminary Design of a Cold Atom Interferometer for Space Gravity Gradiometry.” *Classical and Quantum Gravity* 36 (21): 215004. <https://doi.org/10.1088/1361-6382/ab4548>.
- Visser, P.N.A.M, and J.A. van den IJssel. 2016. “Orbit Determination and Estimation of Non-Gravitational Accelerations for the GOCE Reentry Phase.” *Advances in Space Research* 58 (9): 1840–53. <https://doi.org/10.1016/j.asr.2016.07.013>.
- Zhu, Zhu, He Liao, Haibo Tu, Xiaochun Duan, and Yanbin Zhao. 2022. “Spaceborne Atom-Interferometry Gravity Gradiometry Design towards Future Satellite Gradiometric Missions.” *Aerospace* 9 (5): 253. <https://doi.org/10.3390/aerospace9050253>.
- Zingerle, P, T Gruber, R Pail, and I Daras. 2014. “Constellation Design and Performance of Future Quantum Satellite Gravity Missions.” *Earth, Planets and Space*.